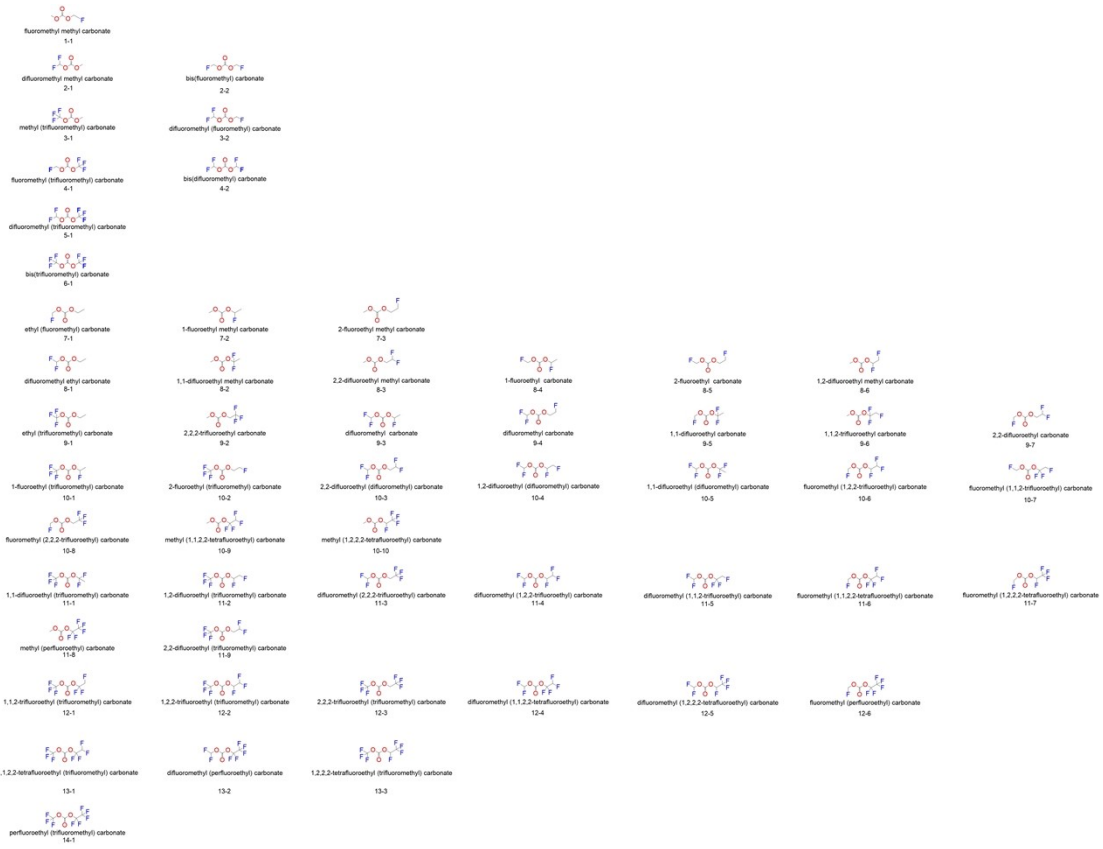

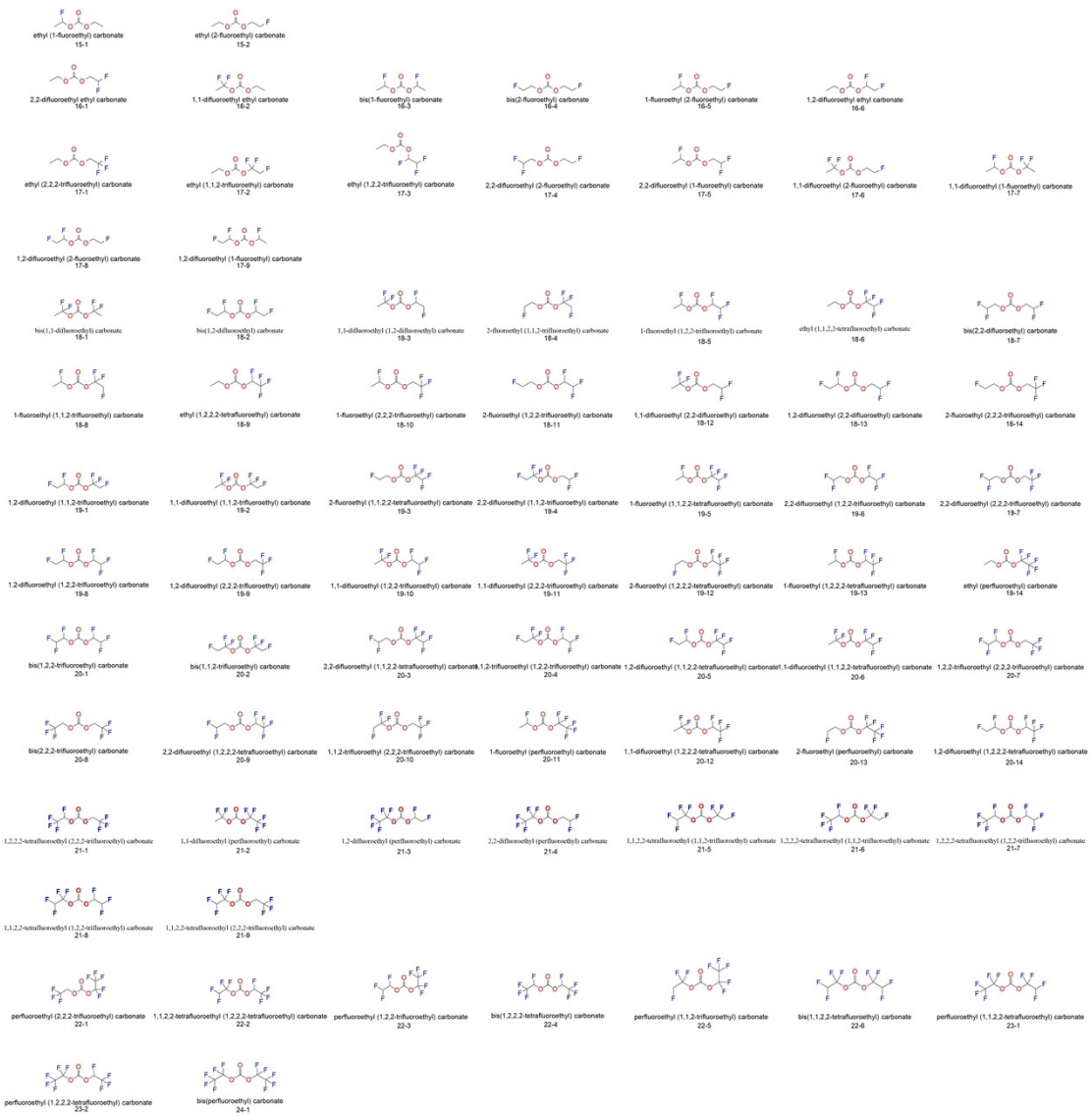

Fig. S1. All molecular structures and nomenclatures

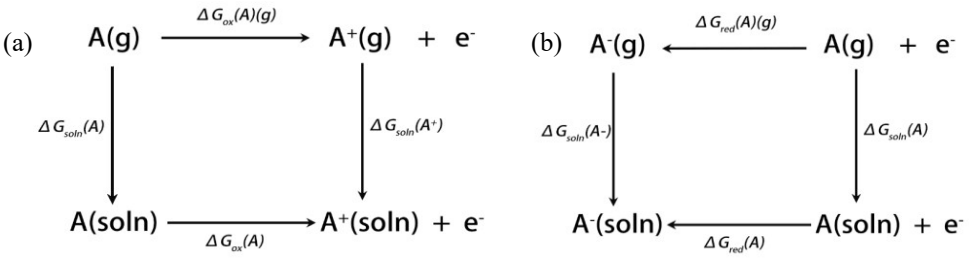

Fig. S2. Thermodynamic cycles for the redox reaction. (a) Oxidation reaction process. (b) Reduction reaction process. Species in the gas phase and in solution are indicated by "(g)" and "(soln)", respectively.

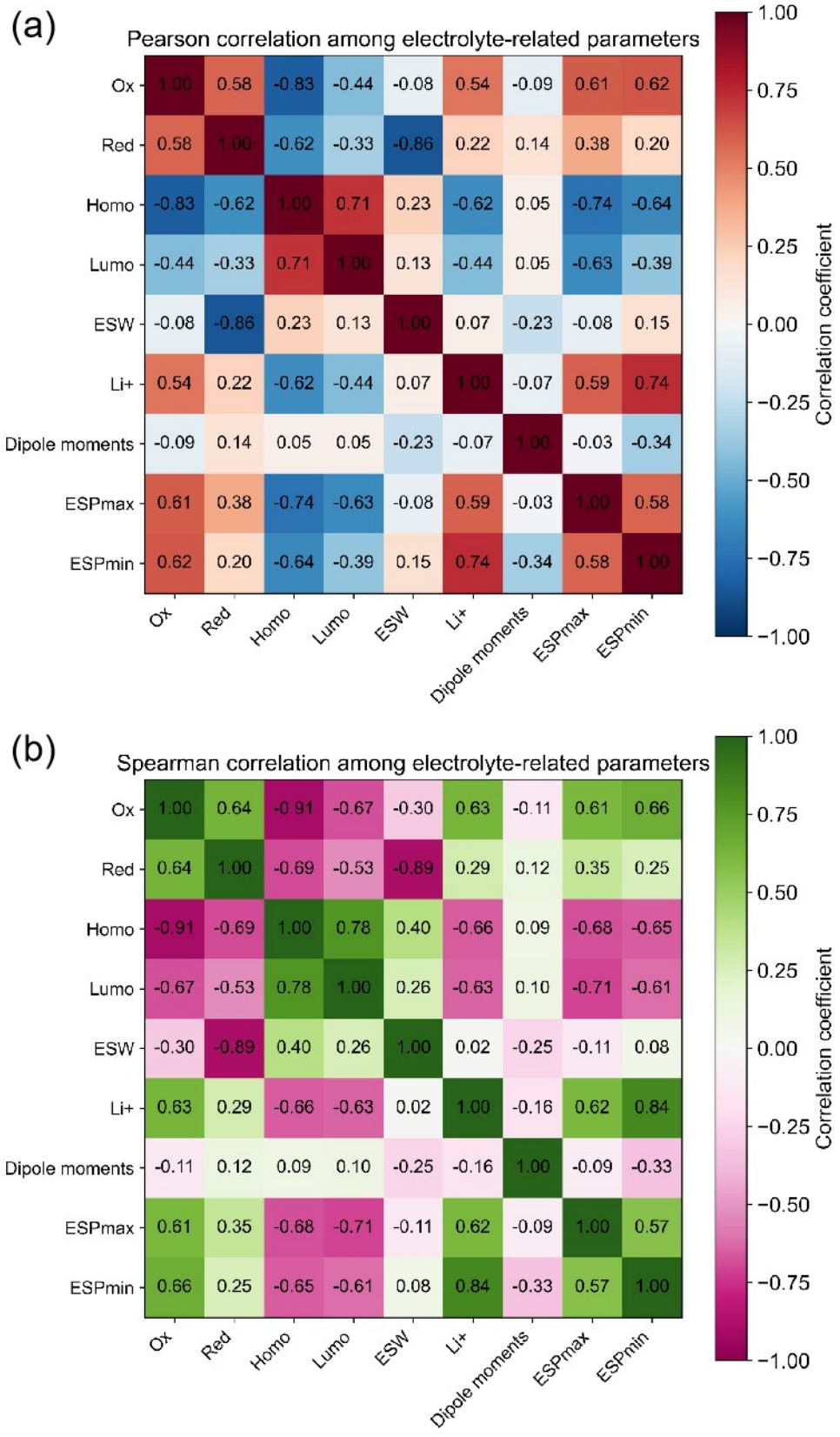

Fig. S3. Correlation analysis among the calculated electrolyte-related parameters.
(a) Pearson correlation matrix. (b) Spearman correlation matrix. Pearson coefficients evaluate linear correlations, while Spearman coefficients evaluate monotonic correlations.

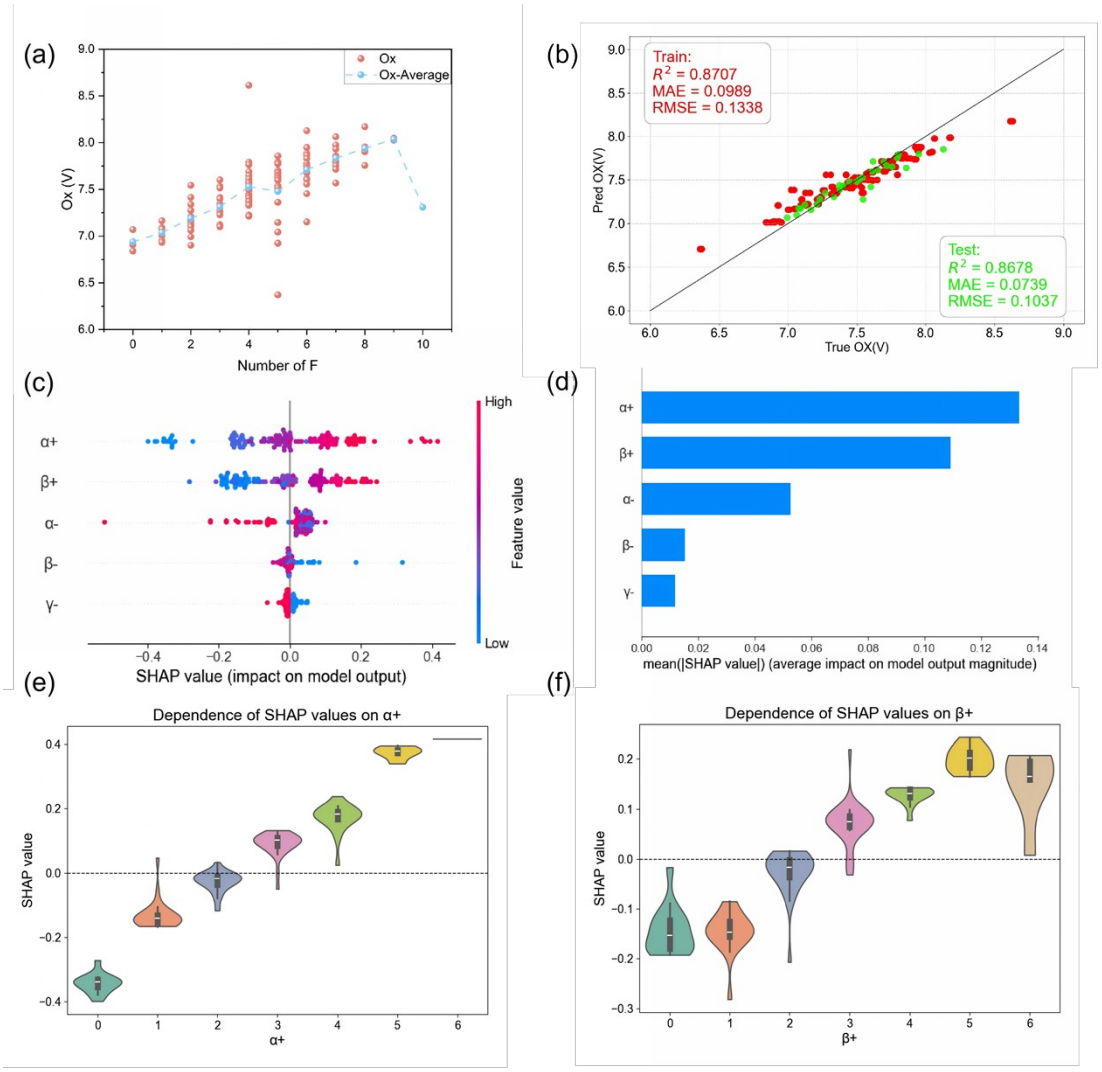

Fig. S4. XGBoost model fitting for the Oxidation potentials of the CFs. (a) Distribution of oxidation potentials under different fluorination conditions. (b) Performance of the machine learning model in fitting and predicting oxidation potentials (with red and green dots representing the training and testing datasets, respectively). (c) SHAP values for all input features, providing local interpretability of the machine learning model. (d) Importance ranking of all input features. (e) Dependence of SHAP values on α+. (f) Dependence of SHAP values on β+.

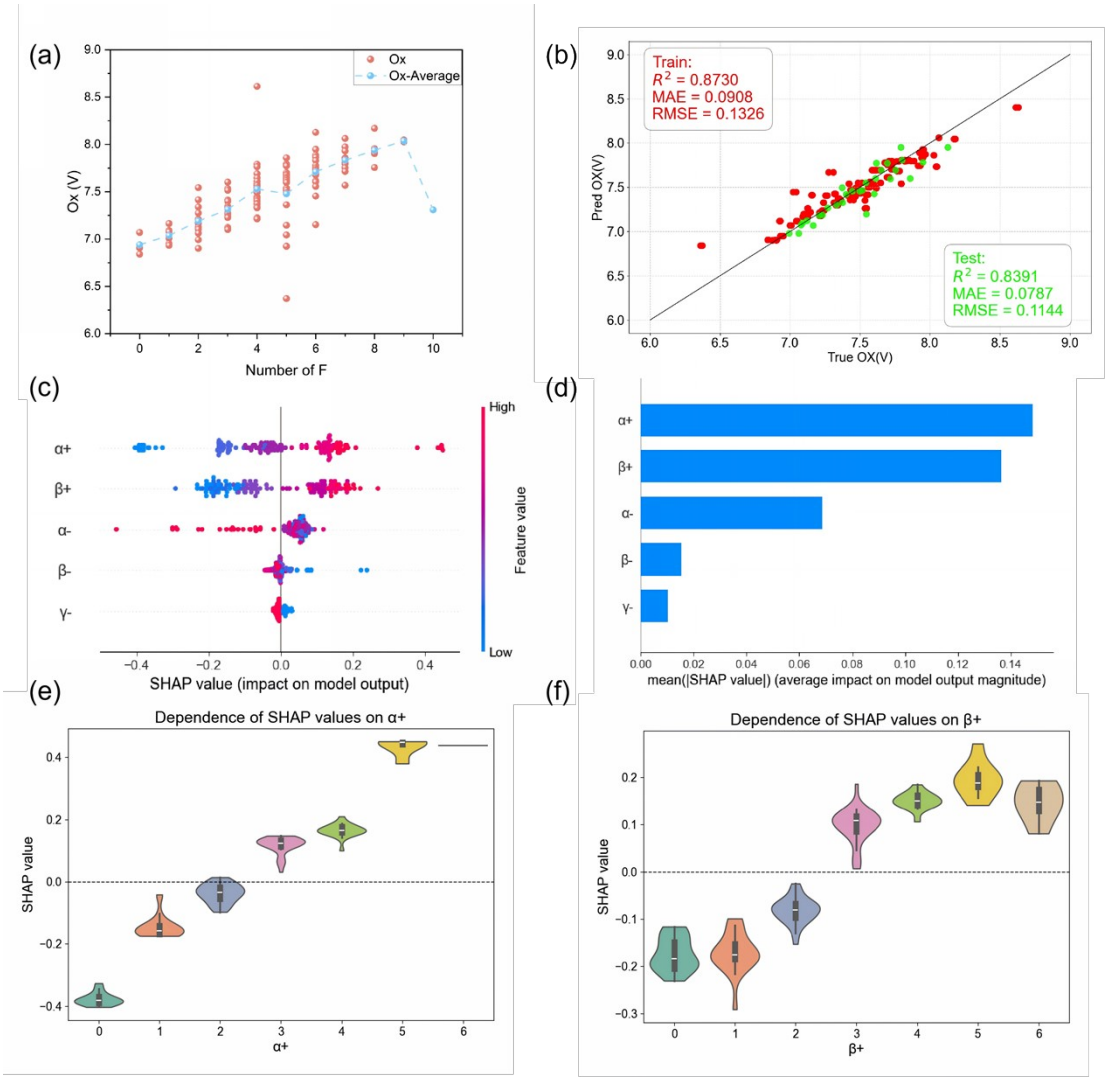

Fig. S5. RF model fitting for the Oxidation potentials of the CFs. (a) Distribution of oxidation potentials under different fluorination conditions. (b) Performance of the machine learning model in fitting and predicting oxidation potentials (with red and green dots representing the training and testing datasets, respectively). (c) SHAP values for all input features, providing local interpretability of the machine learning model. (d) Importance ranking of all input features. (e) Dependence of SHAP values on α+. (f) Dependence of SHAP values on β+.

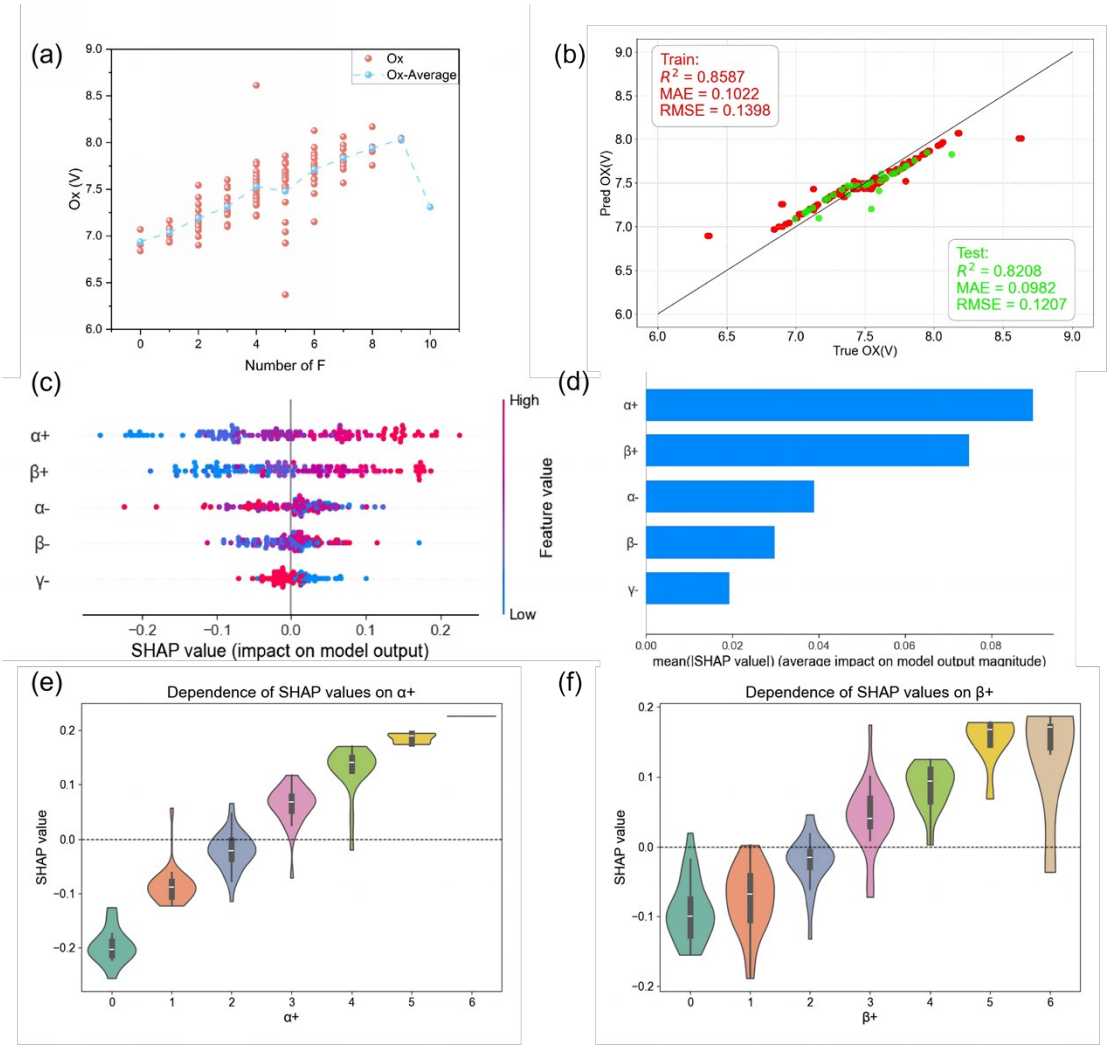

Fig. S6. SVR model fitting for the Oxidation potentials of the CFs. (a) Distribution of oxidation potentials under different fluorination conditions. (b) Performance of the machine learning model in fitting and predicting oxidation potentials (with red and green dots representing the training and testing datasets, respectively). (c) SHAP values for all input features, providing local interpretability of the machine learning model. (d) Importance ranking of all input features. (e) Dependence of SHAP values on α+. (f) Dependence of SHAP values on β+.

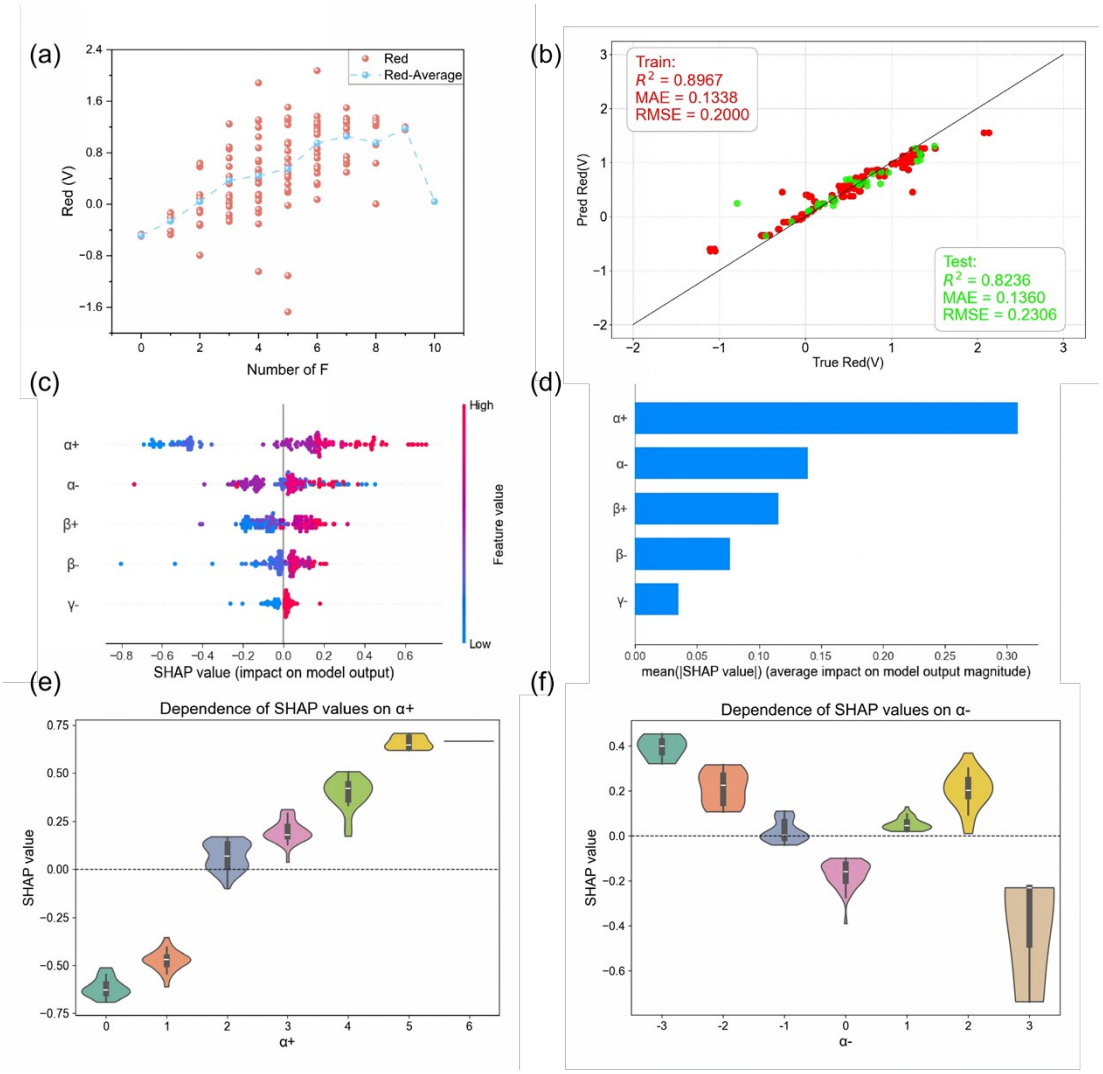

Fig. S7. XGBoost model fitting for the Reduction potentials of the CFs. (a) Distribution of reduction potentials under different fluorination conditions. (b) Performance of the machine learning model in fitting and predicting reduction potentials (with red and green dots representing the training and testing datasets, respectively). (c) SHAP values for all input features, providing local interpretability of the machine learning model. (d) Importance ranking of all input features. (e) Dependence of SHAP values on α+. (f) Dependence of SHAP values on α-.

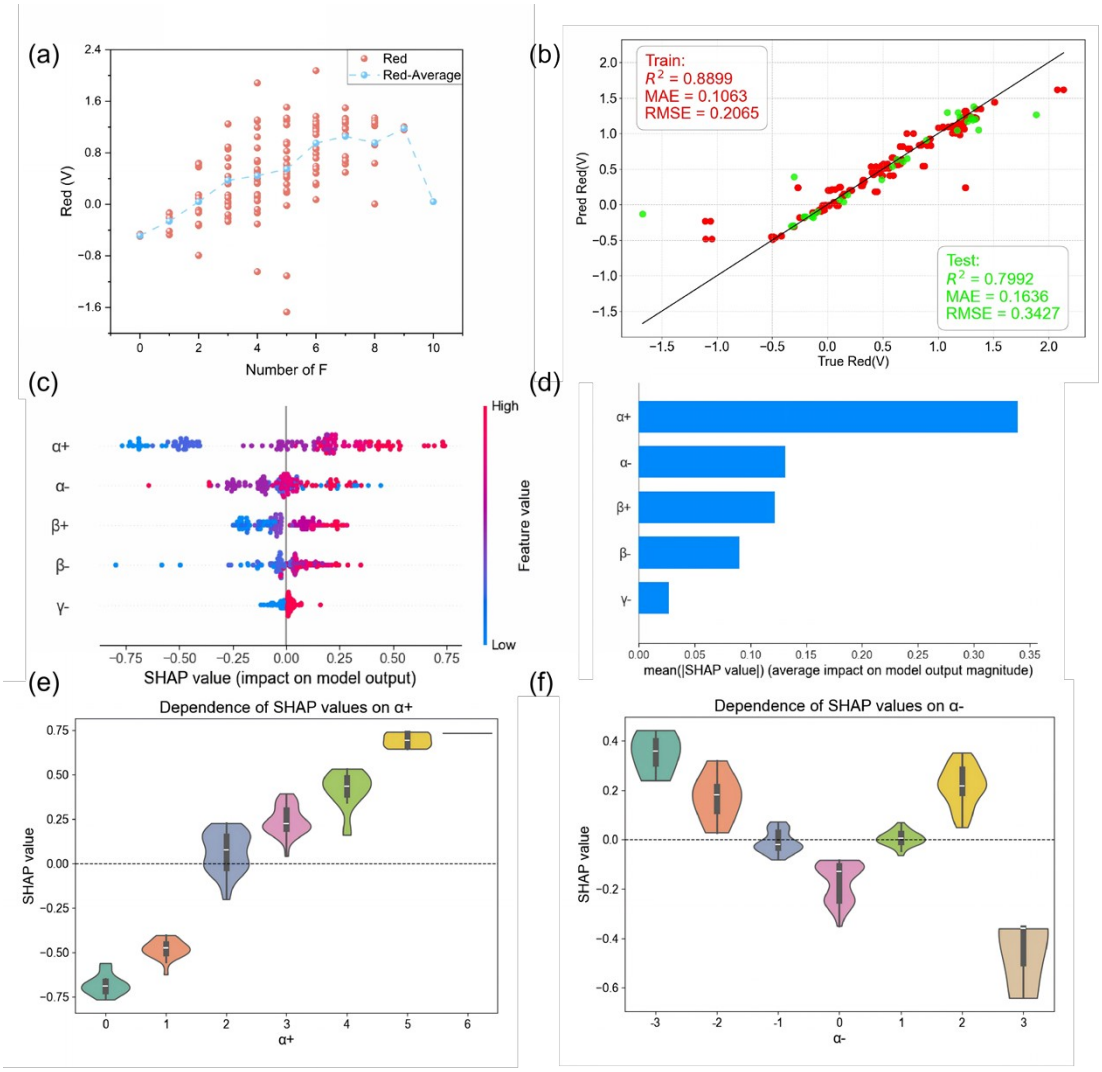

Fig. S8. RF model fitting for the Reduction potentials of the CFs. (a) Distribution of reduction potentials under different fluorination conditions. (b) Performance of the machine learning model in fitting and predicting reduction potentials (with red and green dots representing the training and testing datasets, respectively). (c) SHAP values for all input features, providing local interpretability of the machine learning model. (d) Importance ranking of all input features. (e) Dependence of SHAP values on α+. (f) Dependence of SHAP values on α-.

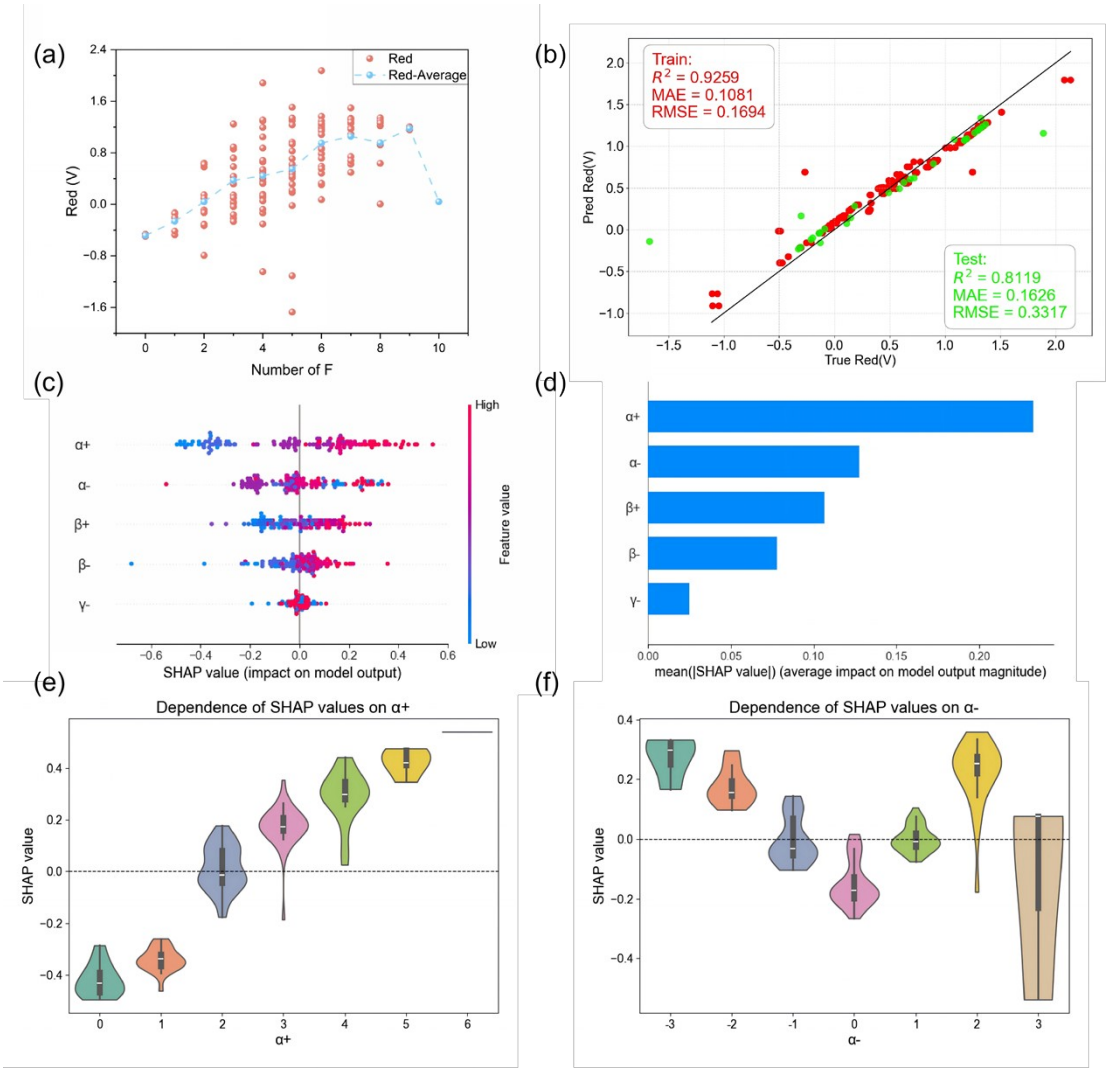

Fig. S9. SVR model fitting for the Reduction potentials of the CFs. (a) Distribution of reduction potentials under different fluorination conditions. (b) Performance of the machine learning model in fitting and predicting reduction potentials (with red and green dots representing the training and testing datasets, respectively). (c) SHAP values for all input features, providing local interpretability of the machine learning model. (d) Importance ranking of all input features. (e) Dependence of SHAP values on α+. (f) Dependence of SHAP values on α-.

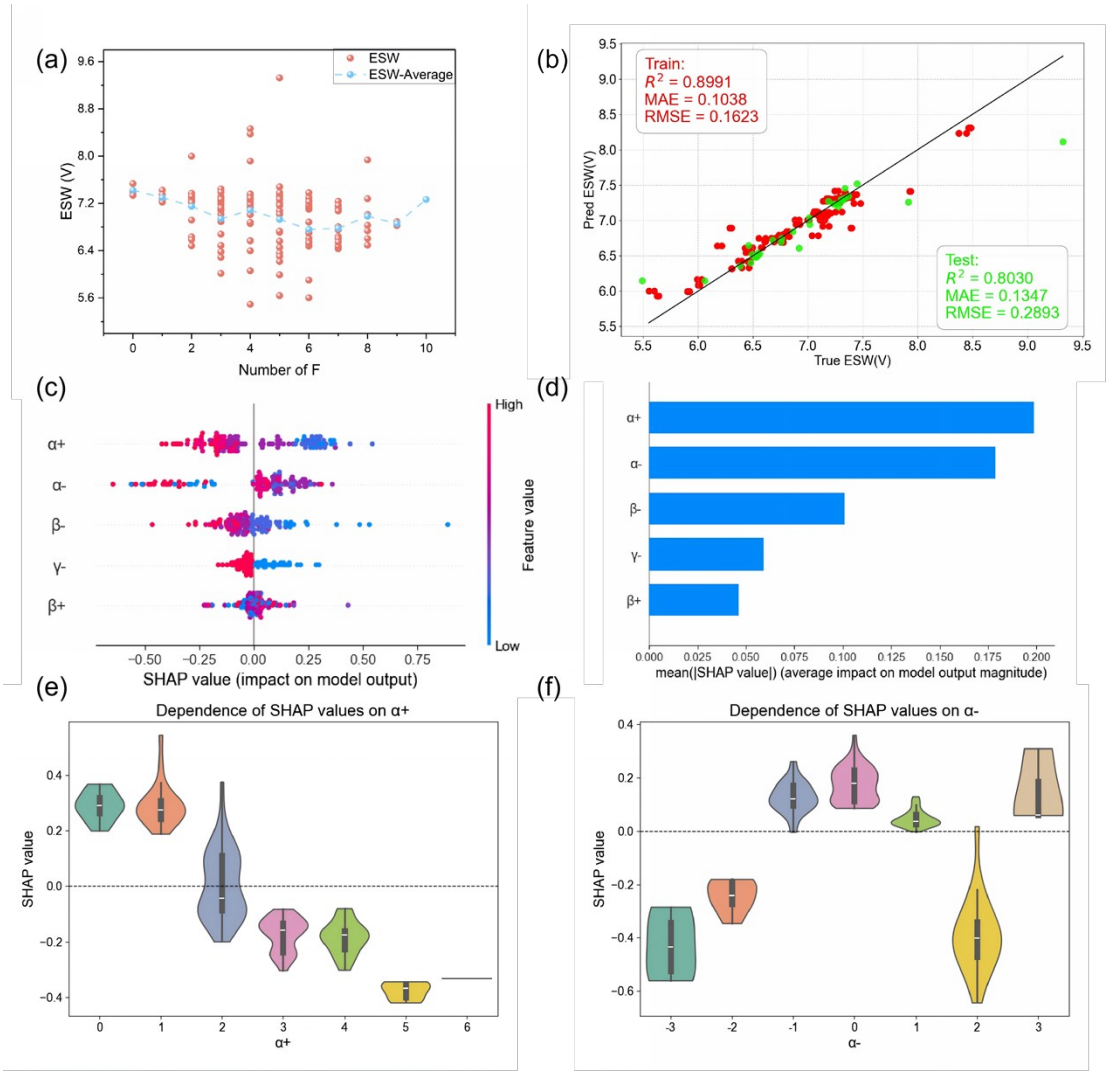

Fig. S10. XGBoost model fitting for the Electrochemical stability windows (ESW) of the CFs. (a) Distribution of electrochemical stability windows under different fluorination conditions. (b) Performance of the machine learning model in fitting and predicting electrochemical stability windows (with red and green dots representing the training and testing datasets, respectively). (c) SHAP values for all input features, providing local interpretability of the machine learning model. (d) Importance ranking of all input features. (e) Dependence of SHAP values on α+. (f) Dependence of SHAP values on α-.

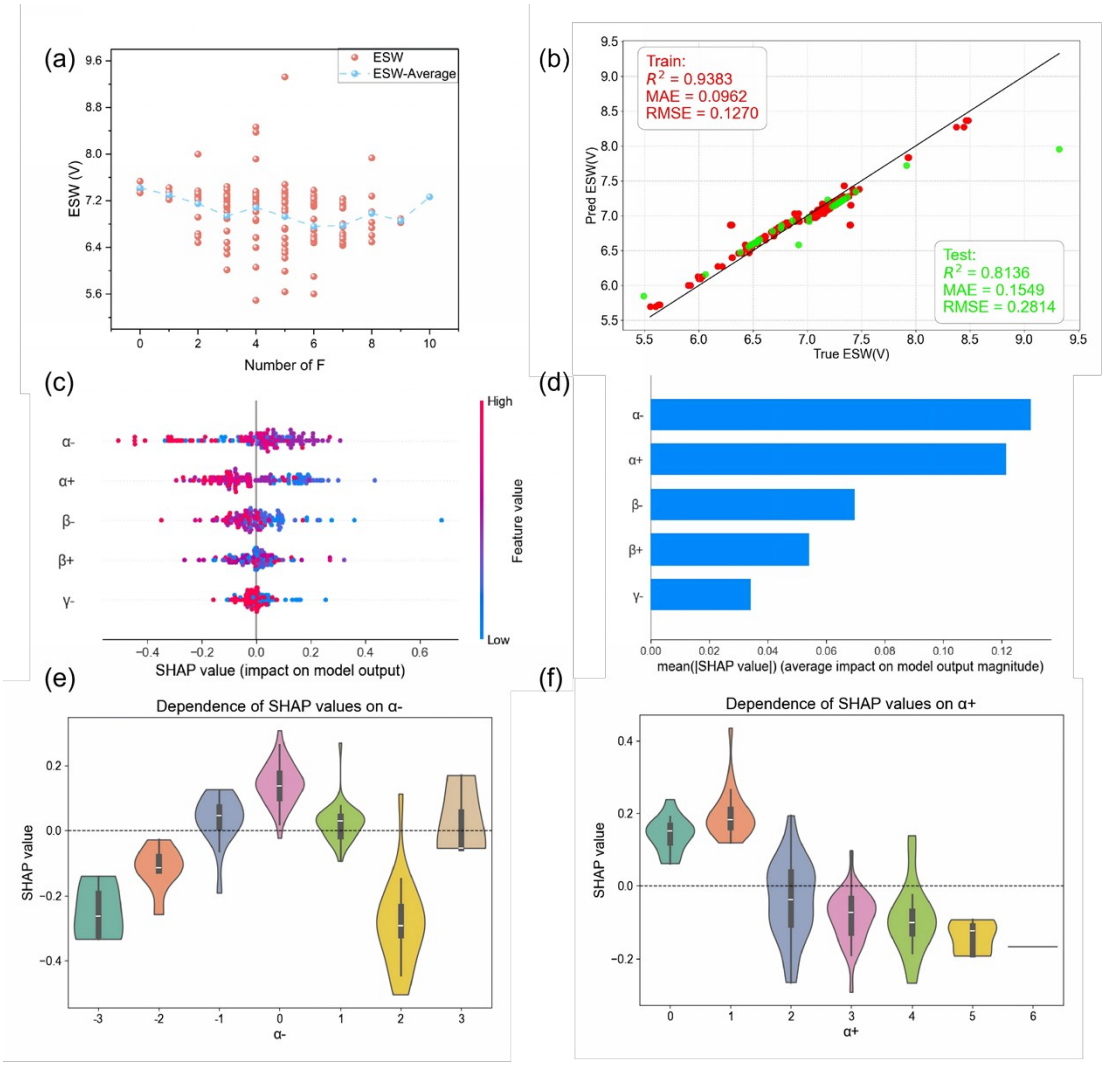

Fig. S11. RF model fitting for the Electrochemical stability windows (ESW) of the CFs. (a) Distribution of electrochemical stability windows under different fluorination conditions. (b) Performance of the machine learning model in fitting and predicting electrochemical stability windows (with red and green dots representing the training and testing datasets, respectively). (c) SHAP values for all input features, providing local interpretability of the machine learning model. (d) Importance ranking of all input features. (e) Dependence of SHAP values on α-. (f) Dependence of SHAP values on α+.

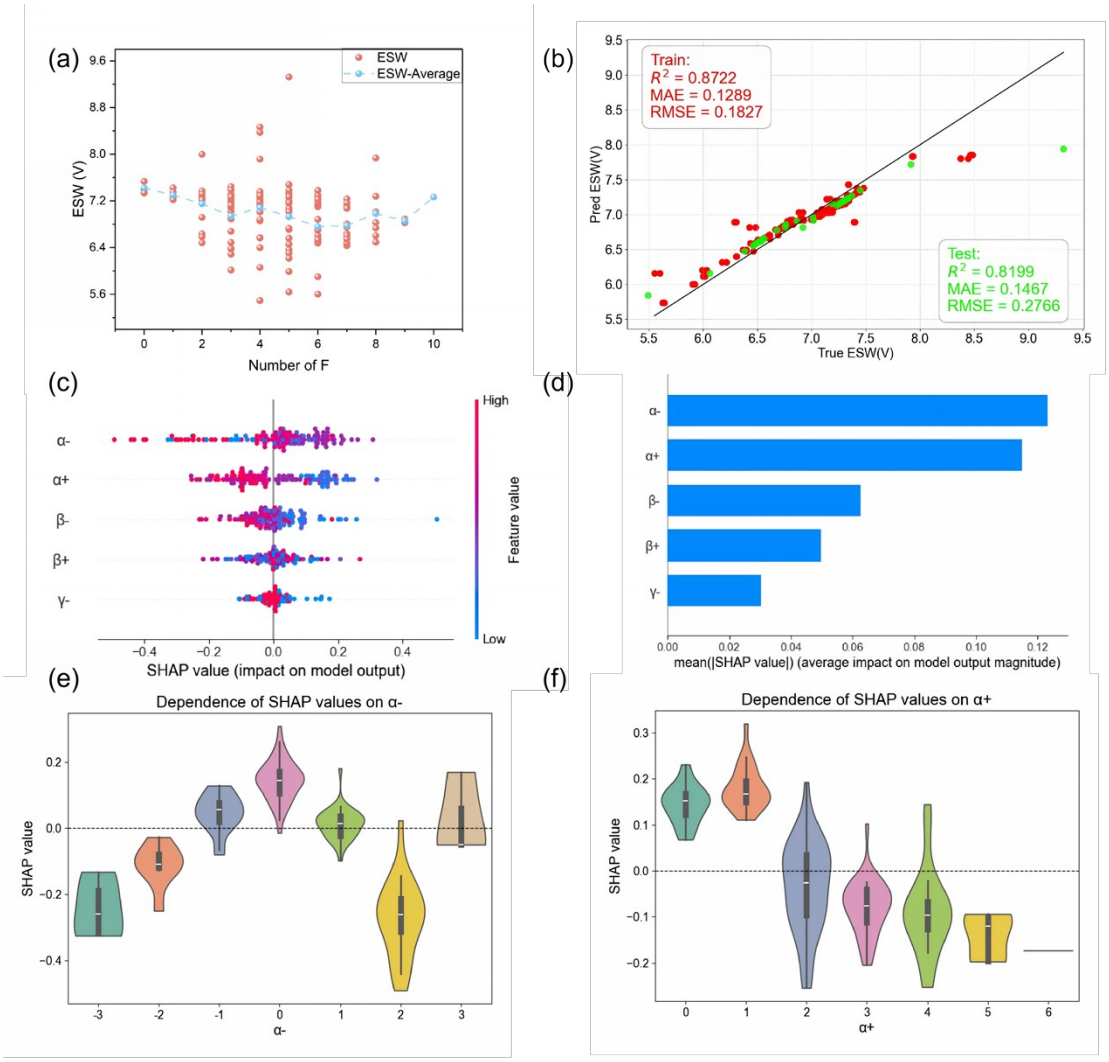

Fig. S12. SVR model fitting for the Electrochemical stability windows (ESW) of the CFs. (a) Distribution of electrochemical stability windows under different fluorination conditions. (b) Performance of the machine learning model in fitting and predicting electrochemical stability windows (with red and green dots representing the training and testing datasets, respectively). (c) SHAP values for all input features, providing local interpretability of the machine learning model. (d) Importance ranking of all input features. (e) Dependence of SHAP values on α-. (f) Dependence of SHAP values on α+.

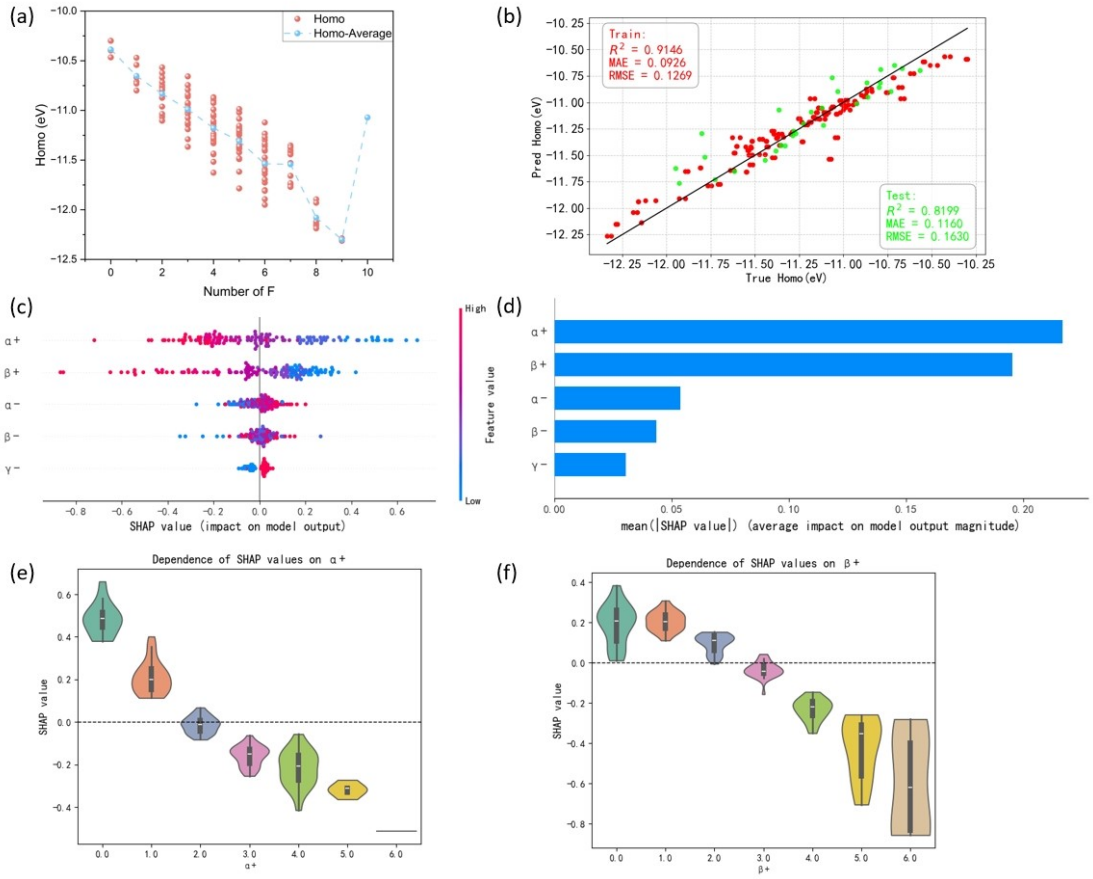

Fig. S13. MLP model fitting for the HOMO of the CFs. (a) Distribution of HOMO under different fluorination conditions. (b) Performance of the machine learning model in fitting and predicting HOMO (with red and green dots representing the training and testing datasets, respectively). (c) SHAP values for all input features, providing local interpretability of the machine learning model. (d) Importance ranking of all input features. (e) Dependence of SHAP values on α+. (f) Dependence of SHAP values on β+.

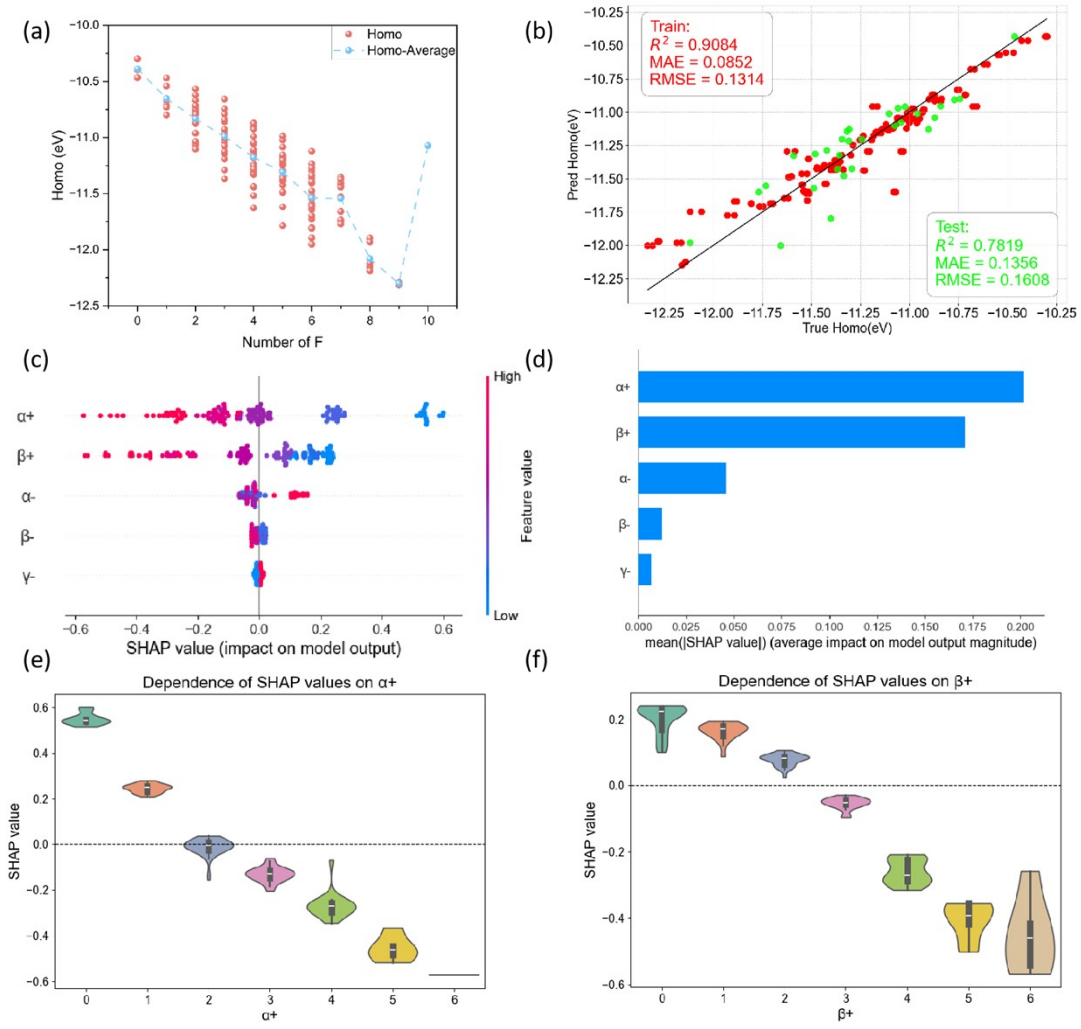

Fig. S14. XGBoost model fitting for the HOMO of the CFs. (a) Distribution of HOMO under different fluorination conditions. (b) Performance of the machine learning model in fitting and predicting HOMO (with red and green dots representing the training and testing datasets, respectively). (c) SHAP values for all input features, providing local interpretability of the machine learning model. (d) Importance ranking of all input features. (e) Dependence of SHAP values on α+. (f) Dependence of SHAP values on β+.

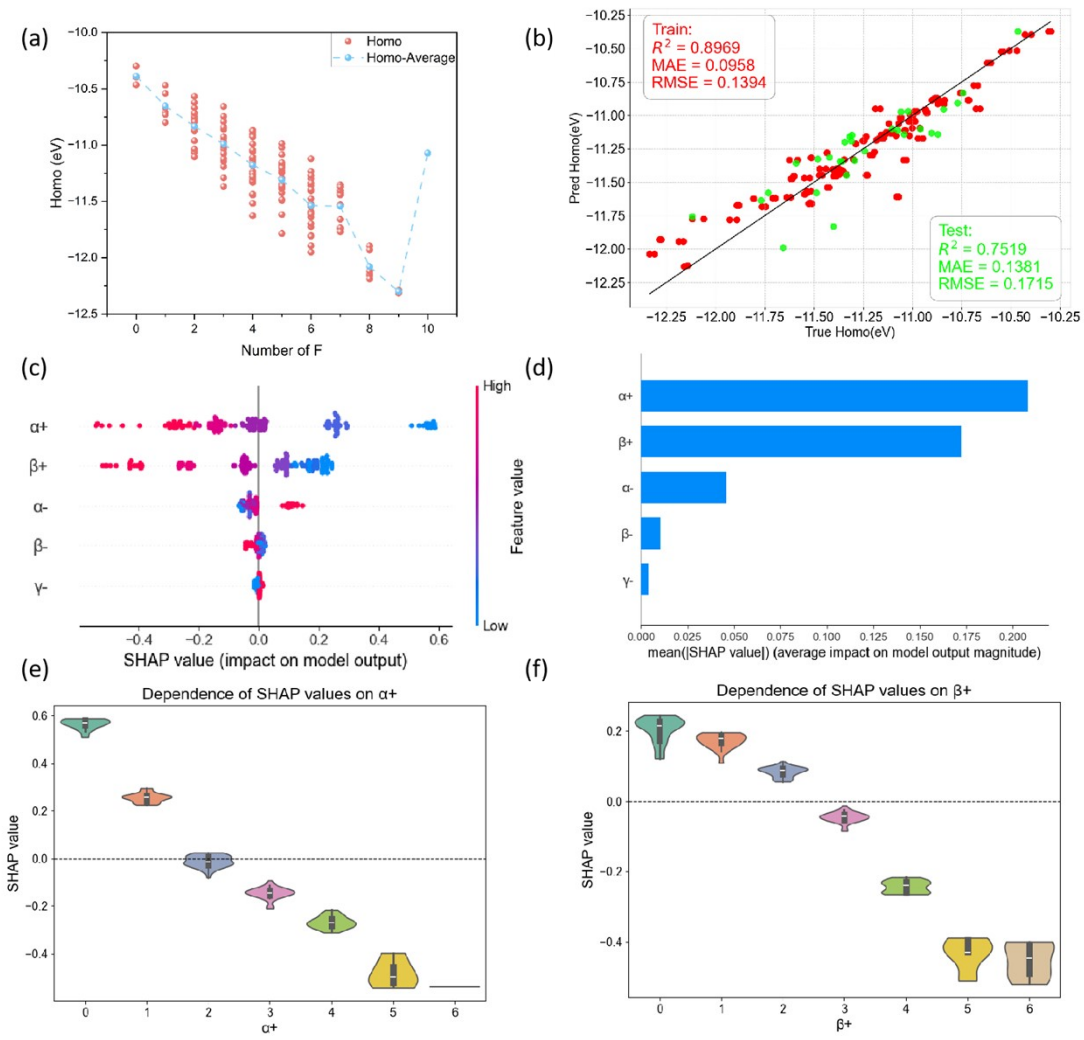

Fig. S15. RF model fitting for the HOMO of the CFs. (a) Distribution of HOMO under different fluorination conditions. (b) Performance of the machine learning model in fitting and predicting HOMO (with red and green dots representing the training and testing datasets, respectively). (c) SHAP values for all input features, providing local interpretability of the machine learning model. (d) Importance ranking of all input features. (e) Dependence of SHAP values on α+. (f) Dependence of SHAP values on β+.

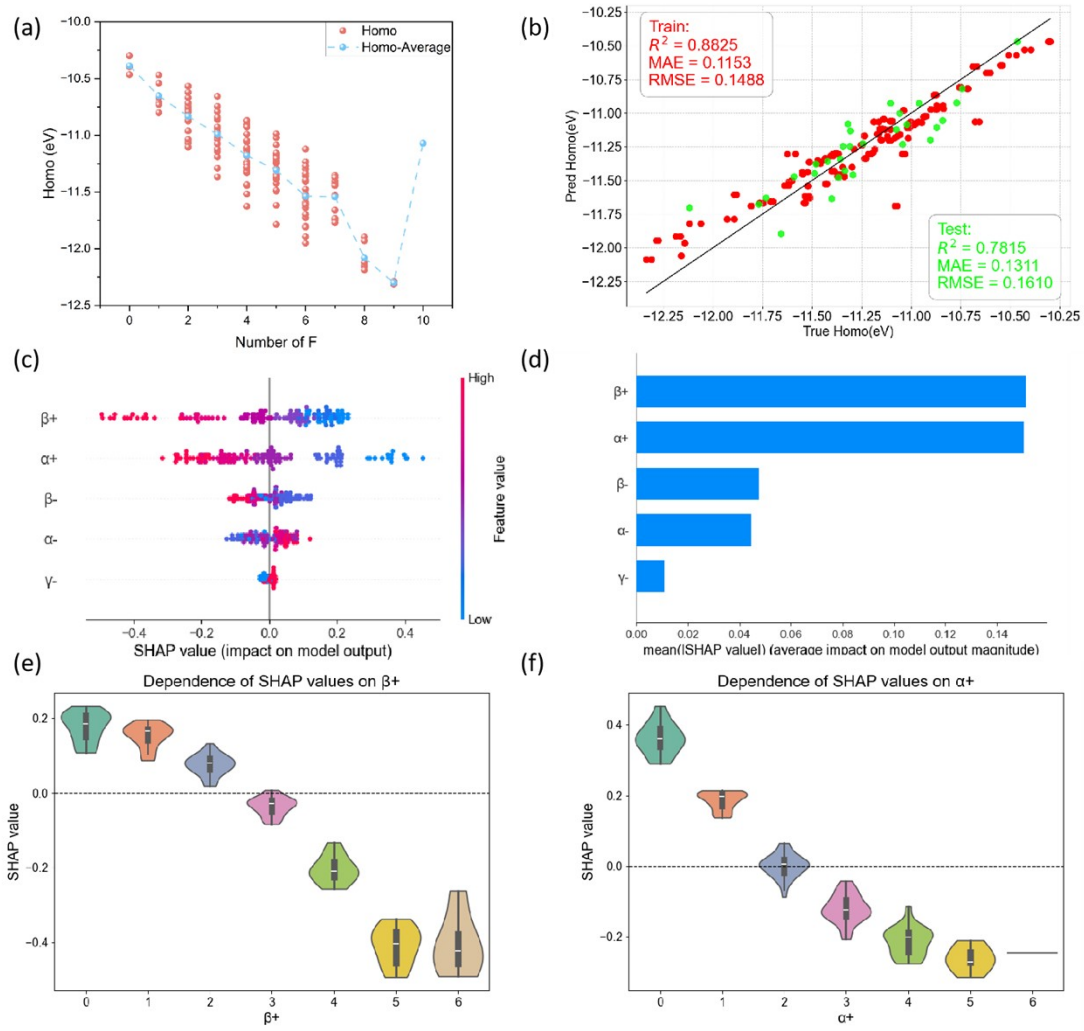

Fig. S16. SVR model fitting for the HOMO of the CFs. (a) Distribution of HOMO under different fluorination conditions. (b) Performance of the machine learning model in fitting and predicting HOMO (with red and green dots representing the training and testing datasets, respectively). (c) SHAP values for all input features, providing local interpretability of the machine learning model. (d) Importance ranking of all input features. (e) Dependence of SHAP values on β+. (f) Dependence of SHAP values on α+.

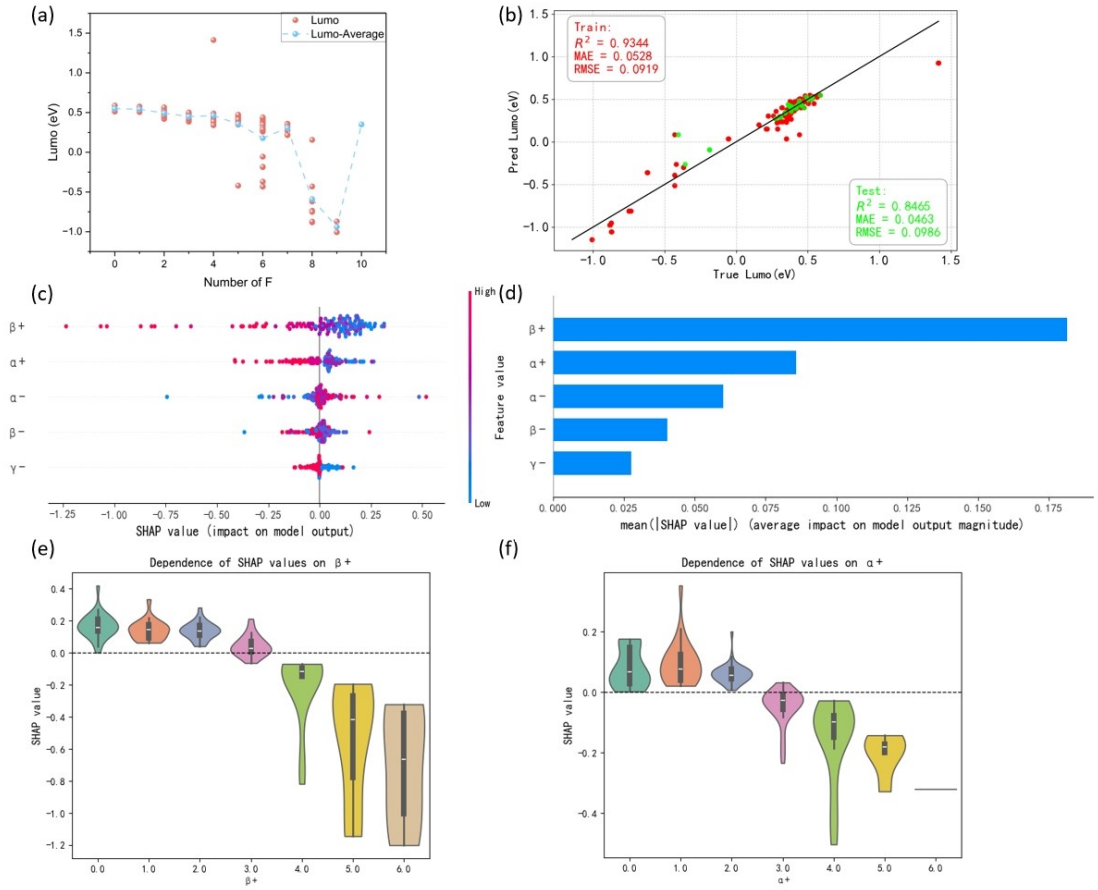

Fig. S17. MLP model fitting for the LUMO of the CFs. (a) Distribution of LUMO under different fluorination conditions. (b) Performance of the machine learning model in fitting and predicting LUMO (with red and green dots representing the training and testing datasets, respectively). (c) SHAP values for all input features, providing local interpretability of the machine learning model. (d) Importance ranking of all input features. (e) Dependence of SHAP values on β+. (f) Dependence of SHAP values on α+.

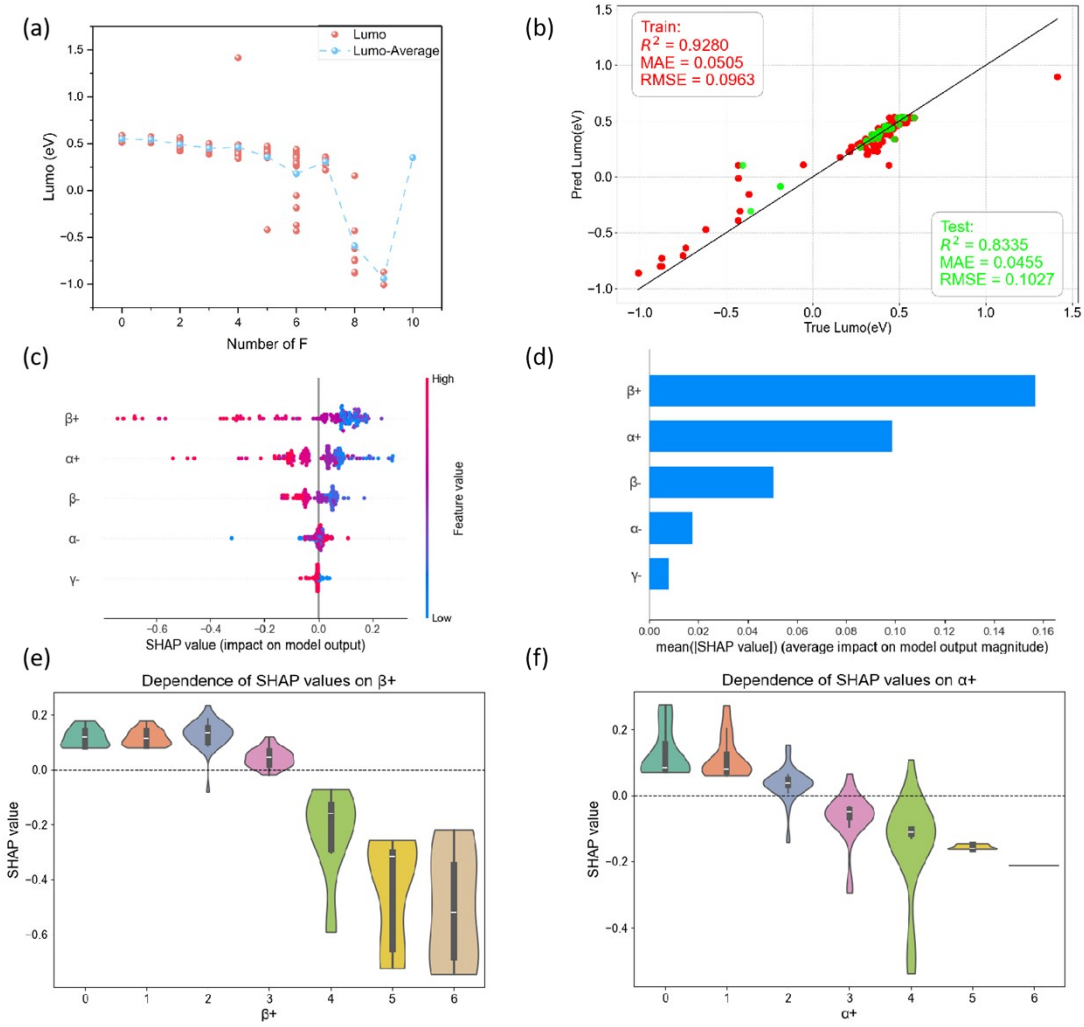

Fig. S18. XGBoost model fitting for the LUMO of the CFs. (a) Distribution of LUMO under different fluorination conditions. (b) Performance of the machine learning model in fitting and predicting LUMO (with red and green dots representing the training and testing datasets, respectively). (c) SHAP values for all input features, providing local interpretability of the machine learning model. (d) Importance ranking of all input features. (e) Dependence of SHAP values on β+. (f) Dependence of SHAP values on α+.

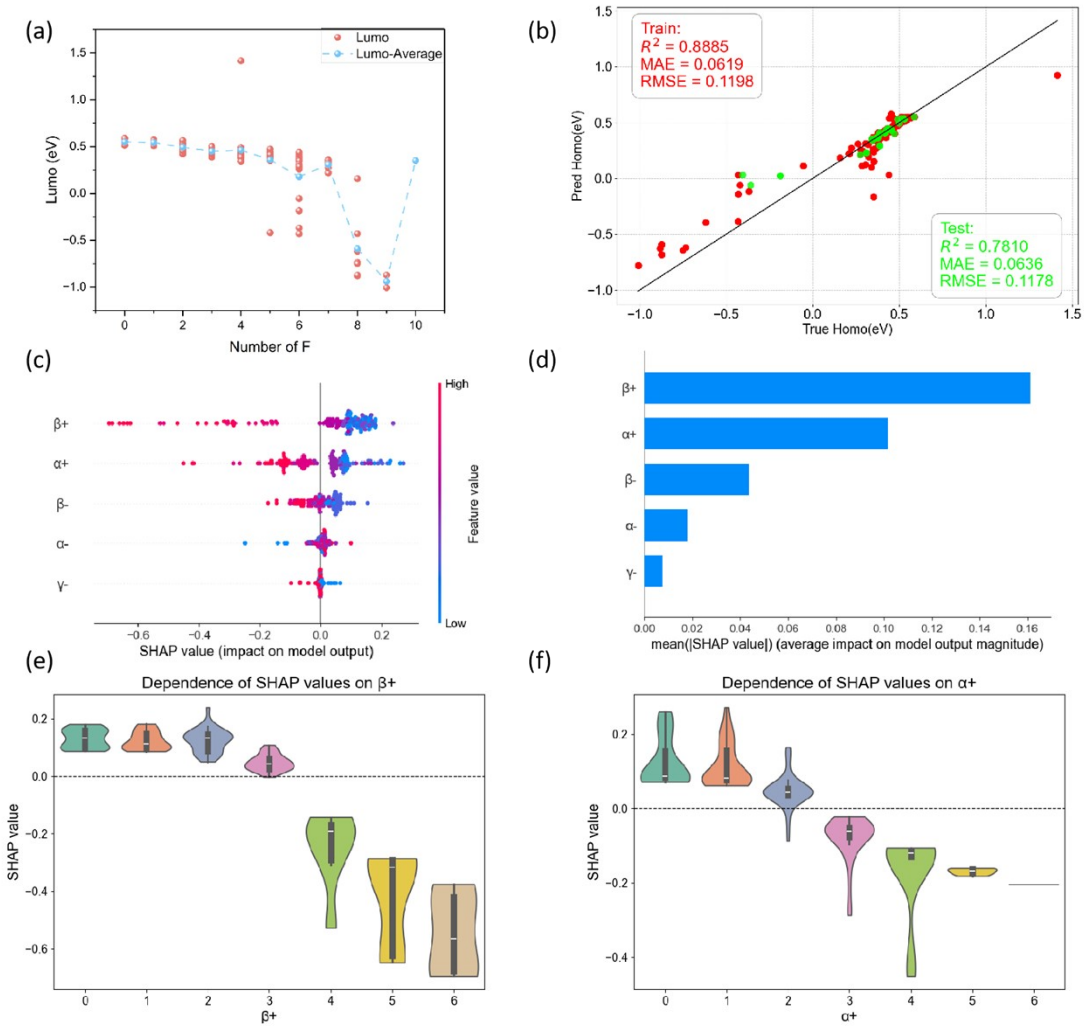

Fig. S19. RF model fitting for the LUMO of the CFs. (a) Distribution of LUMO under different fluorination conditions. (b) Performance of the machine learning model in fitting and predicting LUMO (with red and green dots representing the training and testing datasets, respectively). (c) SHAP values for all input features, providing local interpretability of the machine learning model. (d) Importance ranking of all input features. (e) Dependence of SHAP values on β+. (f) Dependence of SHAP values on α+.

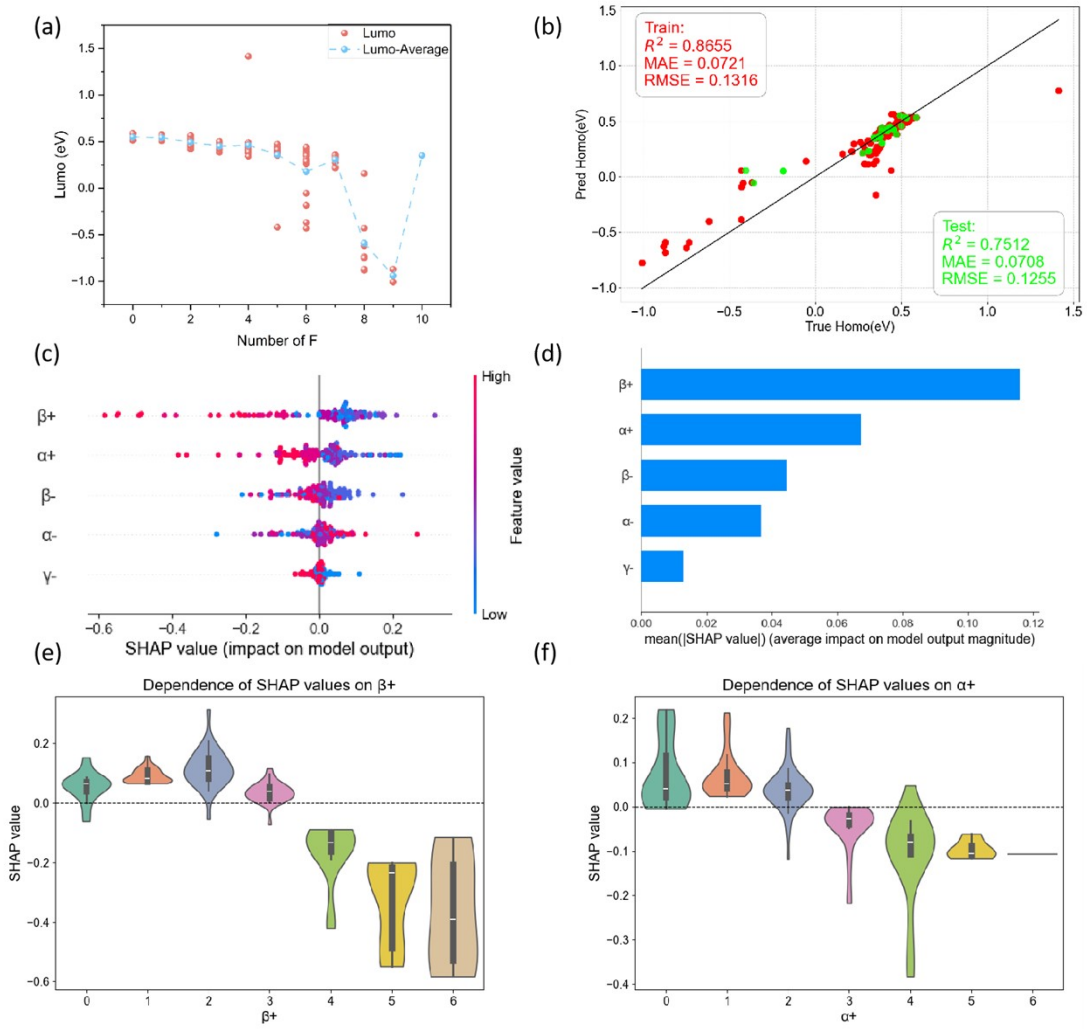

Fig. S20. SVR model fitting for the LUMO of the CFs. (a) Distribution of LUMO under different fluorination conditions. (b) Performance of the machine learning model in fitting and predicting LUMO (with red and green dots representing the training and testing datasets, respectively). (c) SHAP values for all input features, providing local interpretability of the machine learning model. (d) Importance ranking of all input features. (e) Dependence of SHAP values on β+. (f) Dependence of SHAP values on α+.

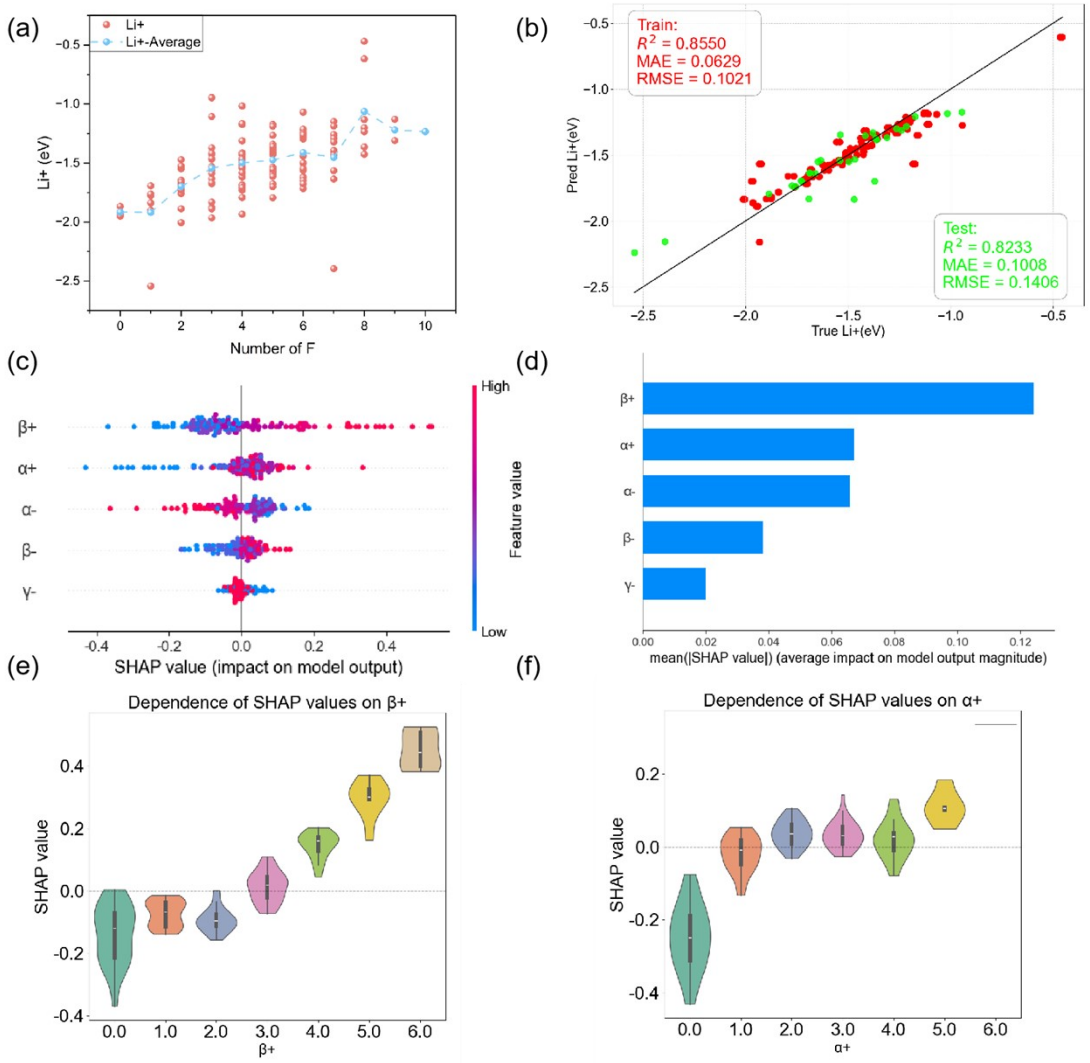

Fig. S21. XGBoost model fitting for the Li^+ binding energies of the CFs. (a) Distribution of Li^+ binding energies under different fluorination conditions. (b) Performance of the machine learning model in fitting and predicting Li^+ binding energies (with red and green dots representing the training and testing datasets, respectively). (c) SHAP values for all input features, providing local interpretability of the machine learning model. (d) Importance ranking of all input features. (e) Dependence of SHAP values on β+. (f) Dependence of SHAP values on α+.

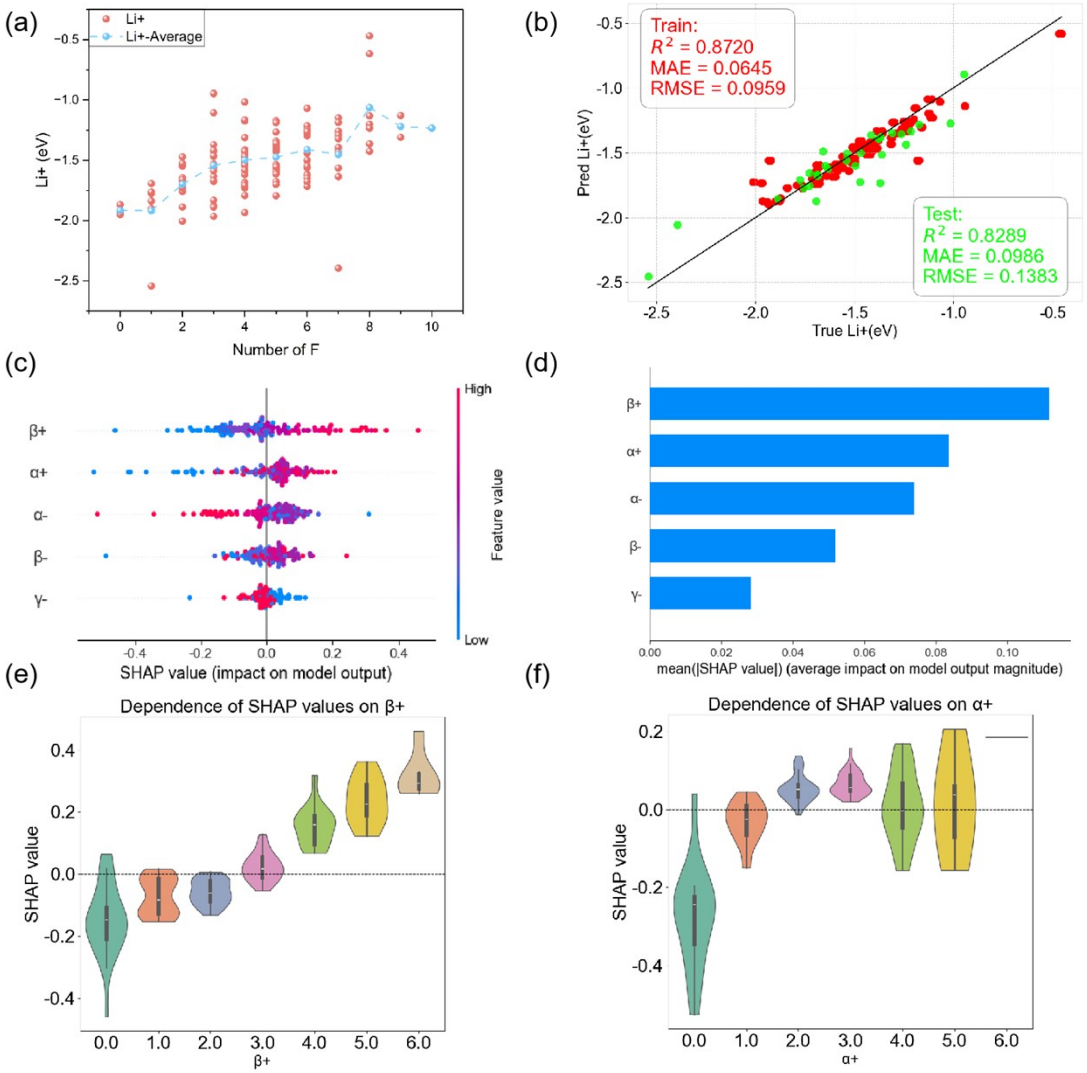

Fig. S22. RF model fitting for the Li^+ binding energies of the CFs. (a) Distribution of Li^+ binding energies under different fluorination conditions. (b) Performance of the machine learning model in fitting and predicting Li^+ binding energies (with red and green dots representing the training and testing datasets, respectively). (c) SHAP values for all input features, providing local interpretability of the machine learning model. (d) Importance ranking of all input features. (e) Dependence of SHAP values on β+. (f) Dependence of SHAP values on α+.

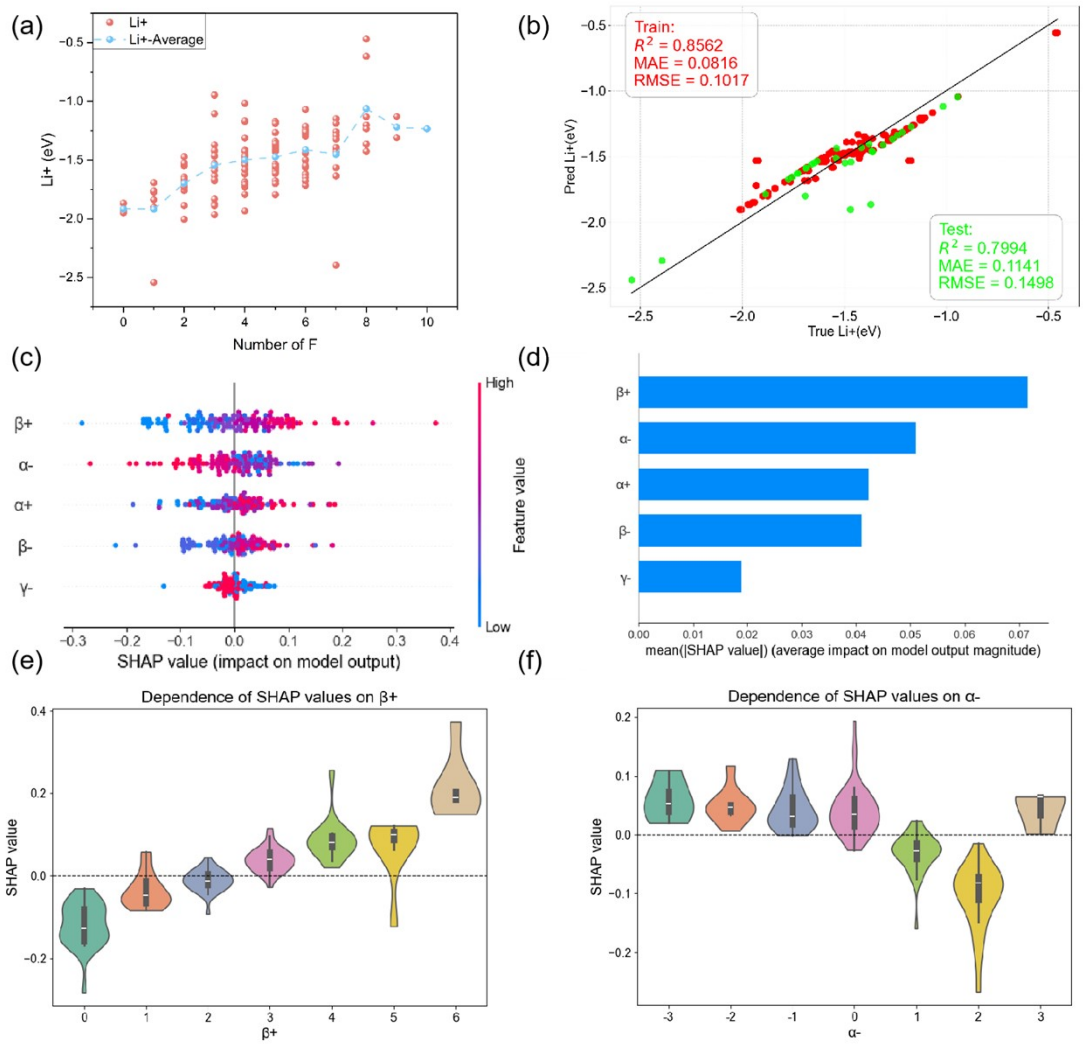

Fig. S23. SVR model fitting for the Li^+ binding energies of the CFs. (a) Distribution of Li^+ binding energies under different fluorination conditions. (b) Performance of the machine learning model in fitting and predicting Li^+ binding energies (with red and green dots representing the training and testing datasets, respectively). (c) SHAP values for all input features, providing local interpretability of the machine learning model. (d) Importance ranking of all input features. (e) Dependence of SHAP values on β+. (f) Dependence of SHAP values on α-.

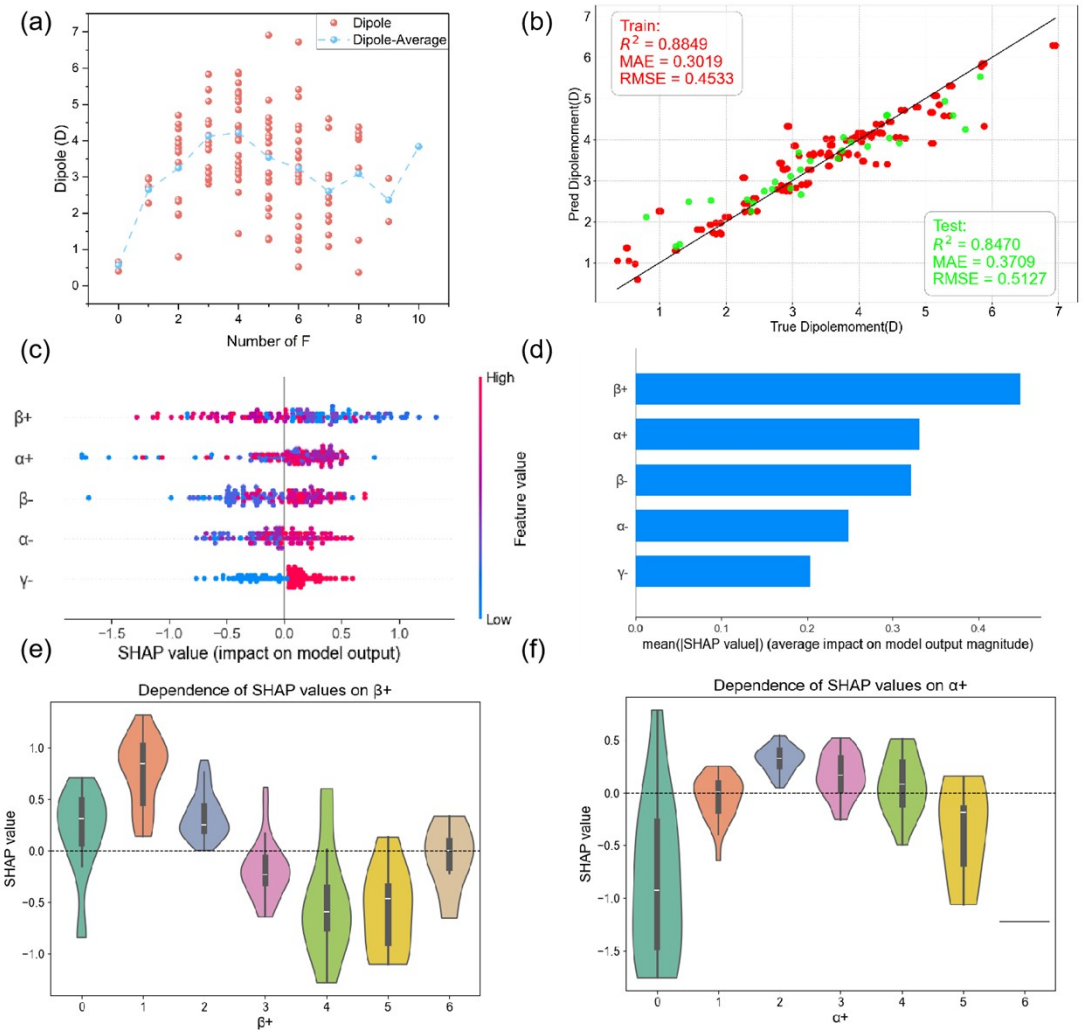

Fig. S24. XGBoost model fitting for the Dipole moments of the CFs. (a) Distribution of dipole moments under different fluorination conditions. (b) Performance of the machine learning model in fitting and predicting dipole moments (with red and green dots representing the training and testing datasets, respectively). (c) SHAP values for all input features, providing local interpretability of the machine learning model. (d) Importance ranking of all input features. (e) Dependence of SHAP values on β+. (f) Dependence of SHAP values on α+.

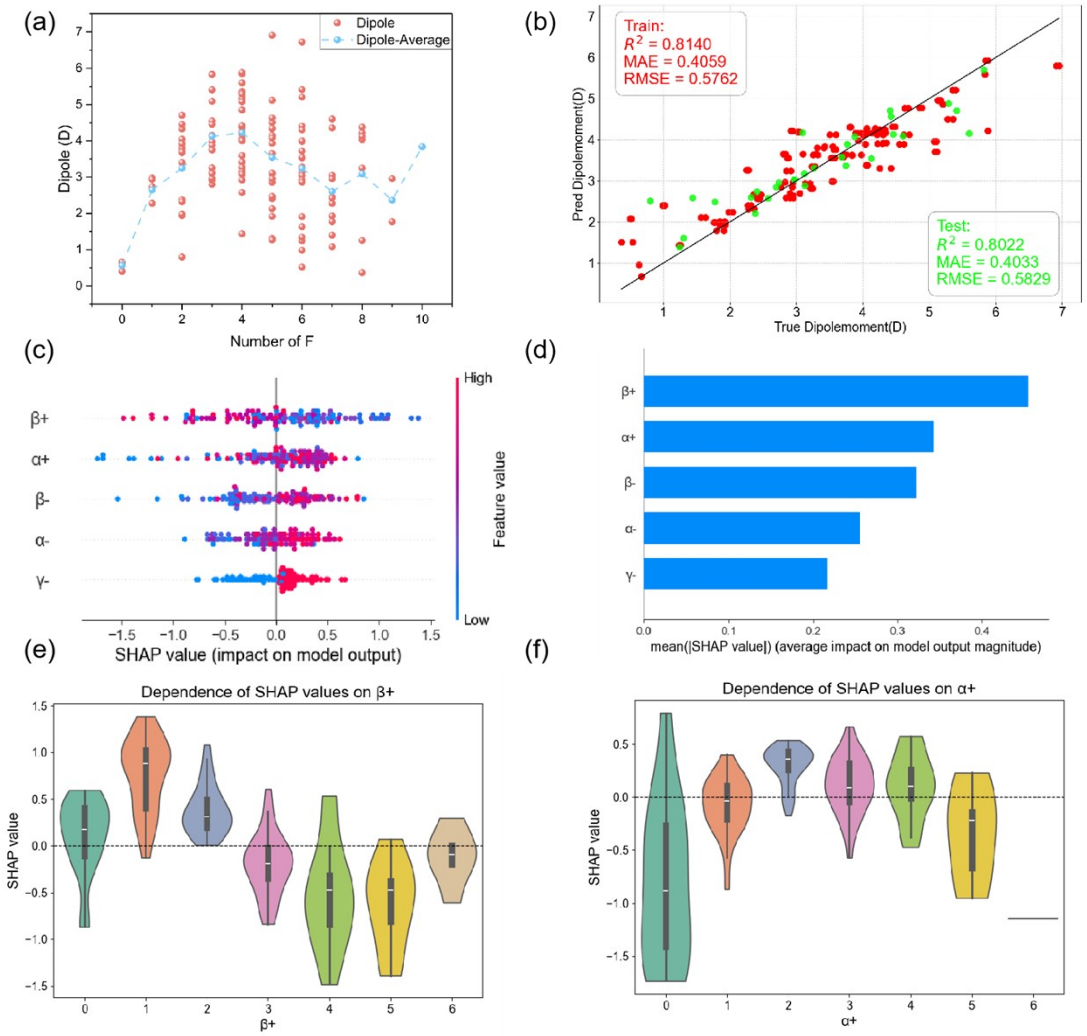

Fig. S25. RF model fitting for the Dipole moments of the CFs. (a) Distribution of dipole moments under different fluorination conditions. (b) Performance of the machine learning model in fitting and predicting dipole moments (with red and green dots representing the training and testing datasets, respectively). (c) SHAP values for all input features, providing local interpretability of the machine learning model. (d) Importance ranking of all input features. (e) Dependence of SHAP values on β+. (f) Dependence of SHAP values on α+.

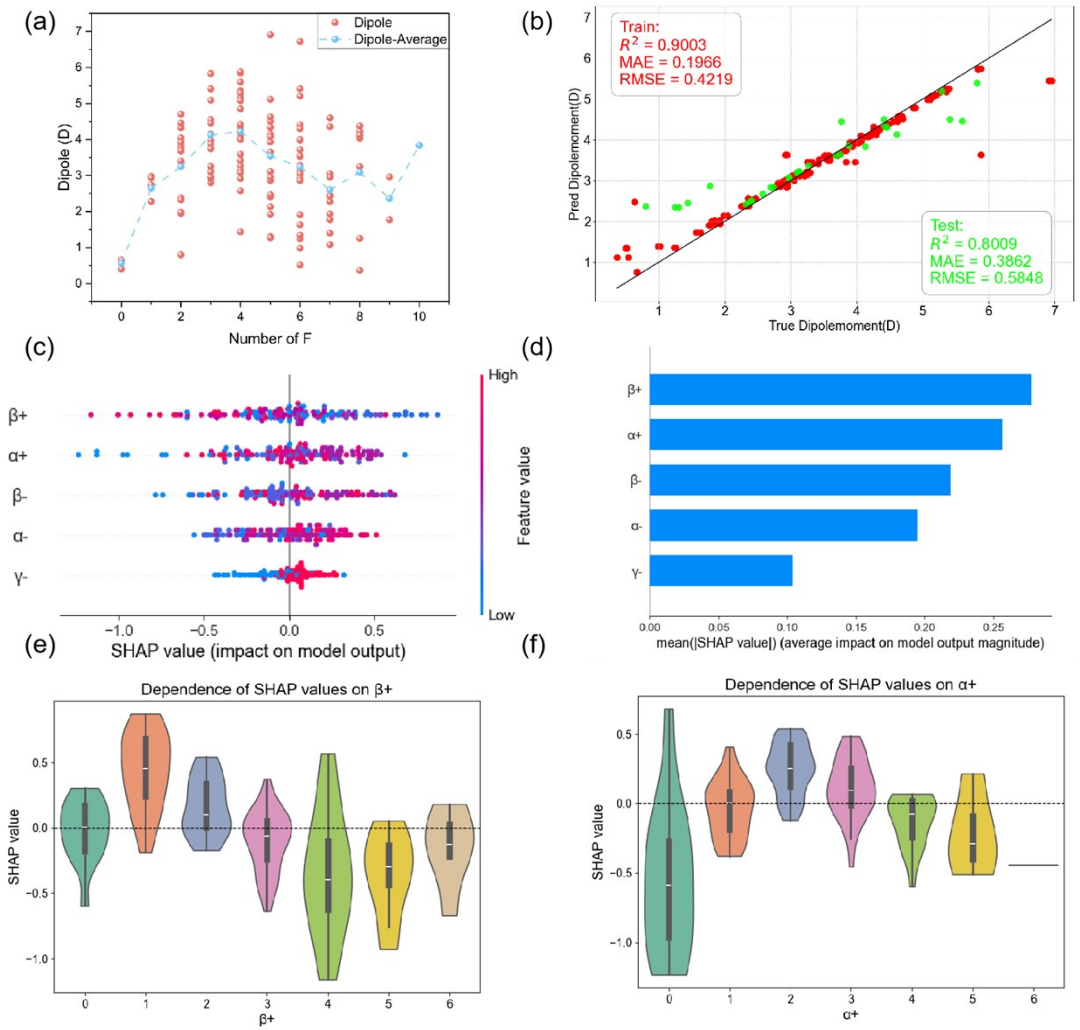

Fig. S26. SVR model fitting for the Dipole moments of the CFs. (a) Distribution of dipole moments under different fluorination conditions. (b) Performance of the machine learning model in fitting and predicting dipole moments (with red and green dots representing the training and testing datasets, respectively). (c) SHAP values for all input features, providing local interpretability of the machine learning model. (d) Importance ranking of all input features. (e) Dependence of SHAP values on β+. (f) Dependence of SHAP values on α+.

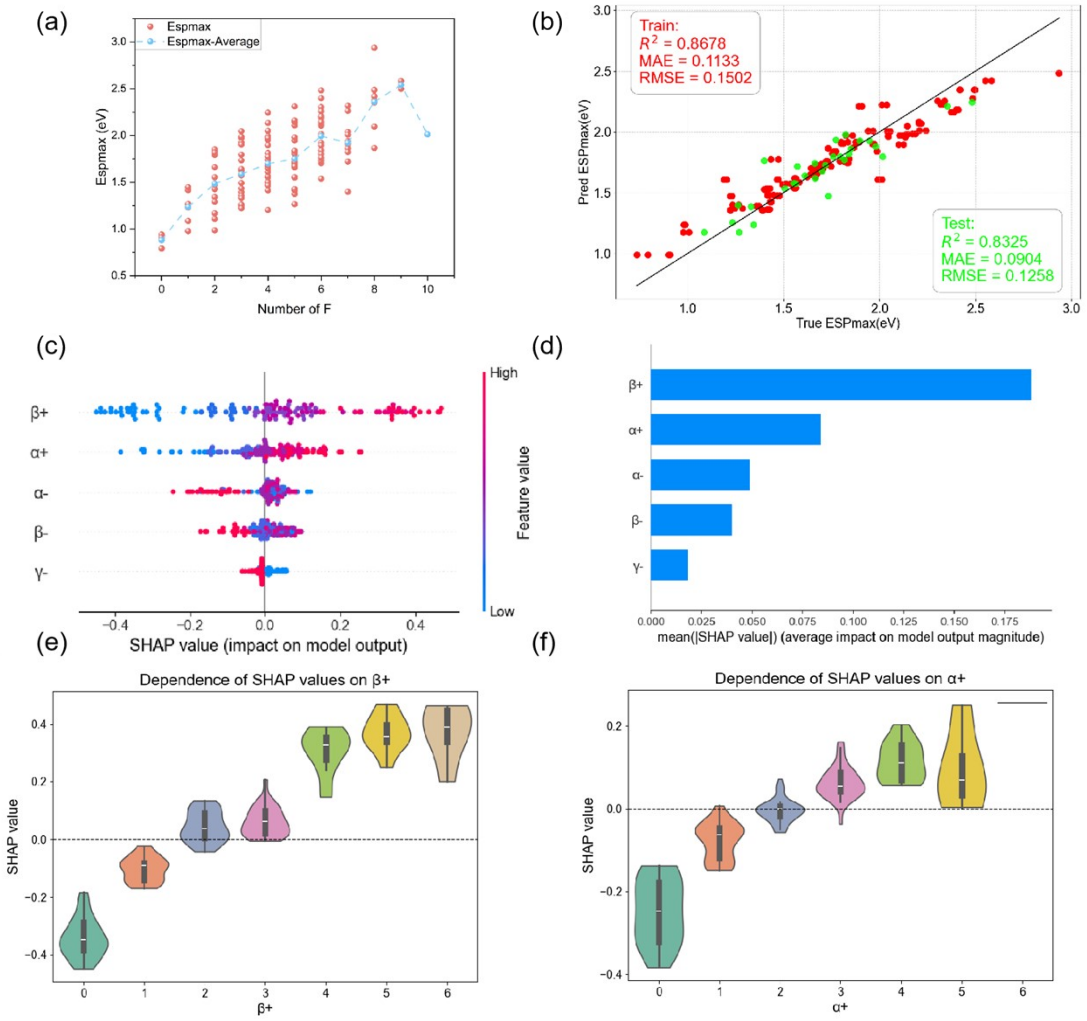

Fig. S27. XGBoost model fitting for the Maximum surface electrostatic potentials of the CFs. (a) Distribution of maximum surface electrostatic potentials under different fluorination conditions. (b) Performance of the machine learning model in fitting and predicting maximum surface electrostatic potentials (with red and green dots representing the training and testing datasets, respectively). (c) SHAP values for all input features, providing local interpretability of the machine learning model. (d) Importance ranking of all input features. (e) Dependence of SHAP values on β+. (f) Dependence of SHAP values on α+.

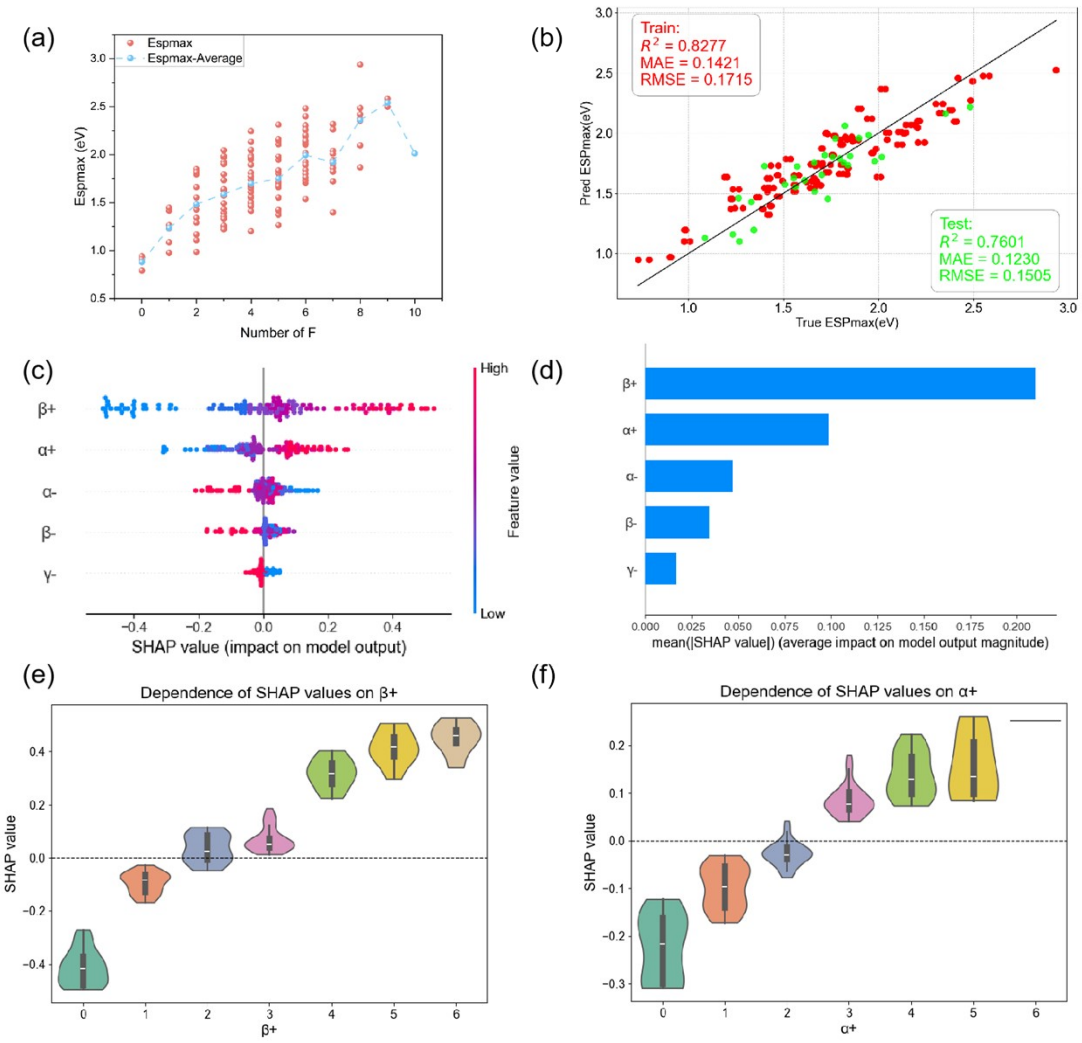

Fig. S28. RF model fitting for the Maximum surface electrostatic potentials of the CFs. (a) Distribution of maximum surface electrostatic potentials under different fluorination conditions. (b) Performance of the machine learning model in fitting and predicting maximum surface electrostatic potentials (with red and green dots representing the training and testing datasets, respectively). (c) SHAP values for all input features, providing local interpretability of the machine learning model. (d) Importance ranking of all input features. (e) Dependence of SHAP values on β+. (f) Dependence of SHAP values on α+.

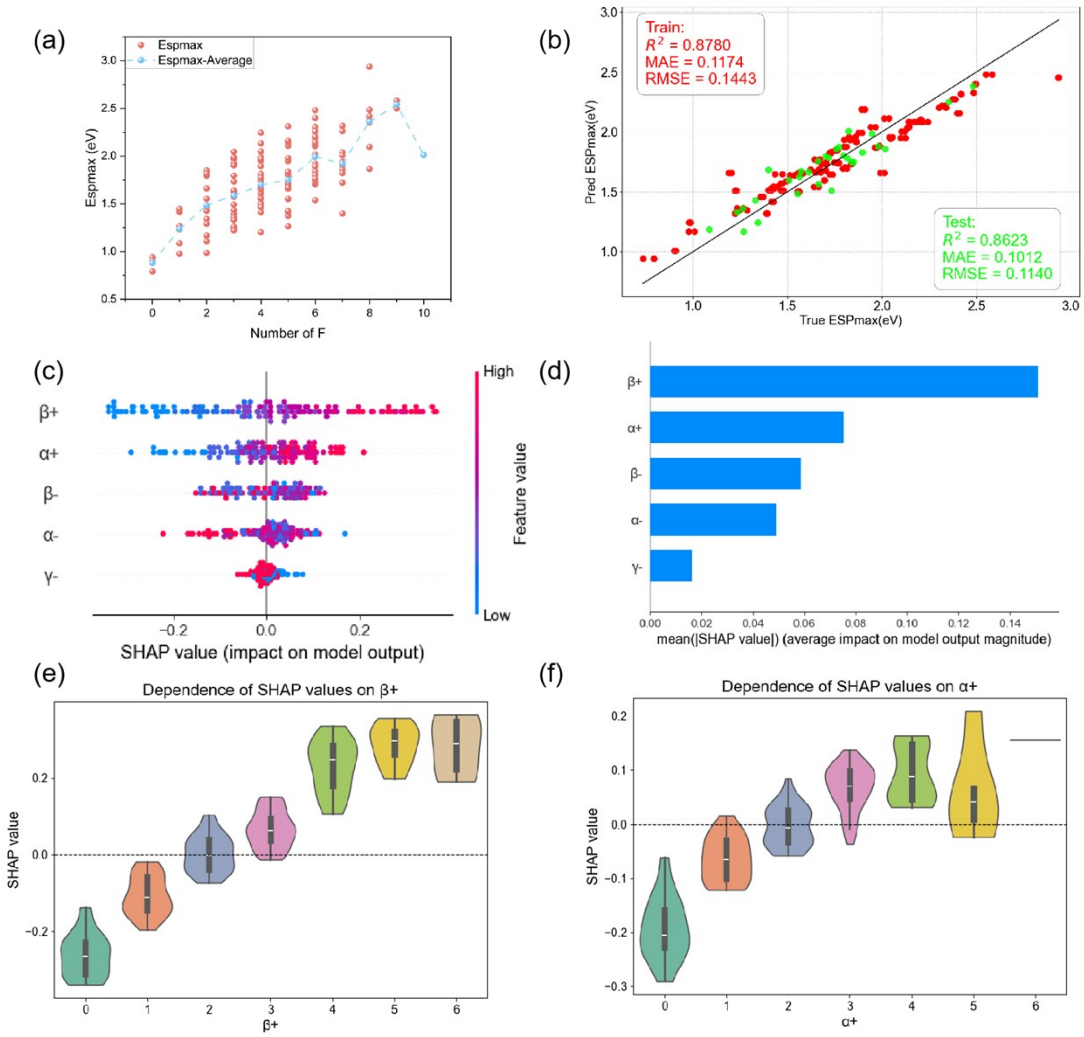

Fig. S29. SVR model fitting for the Maximum surface electrostatic potentials of the CFs. (a) Distribution of maximum surface electrostatic potentials under different fluorination conditions. (b) Performance of the machine learning model in fitting and predicting maximum surface electrostatic potentials (with red and green dots representing the training and testing datasets, respectively). (c) SHAP values for all input features, providing local interpretability of the machine learning model. (d) Importance ranking of all input features. (e) Dependence of SHAP values on β+. (f) Dependence of SHAP values on α+.

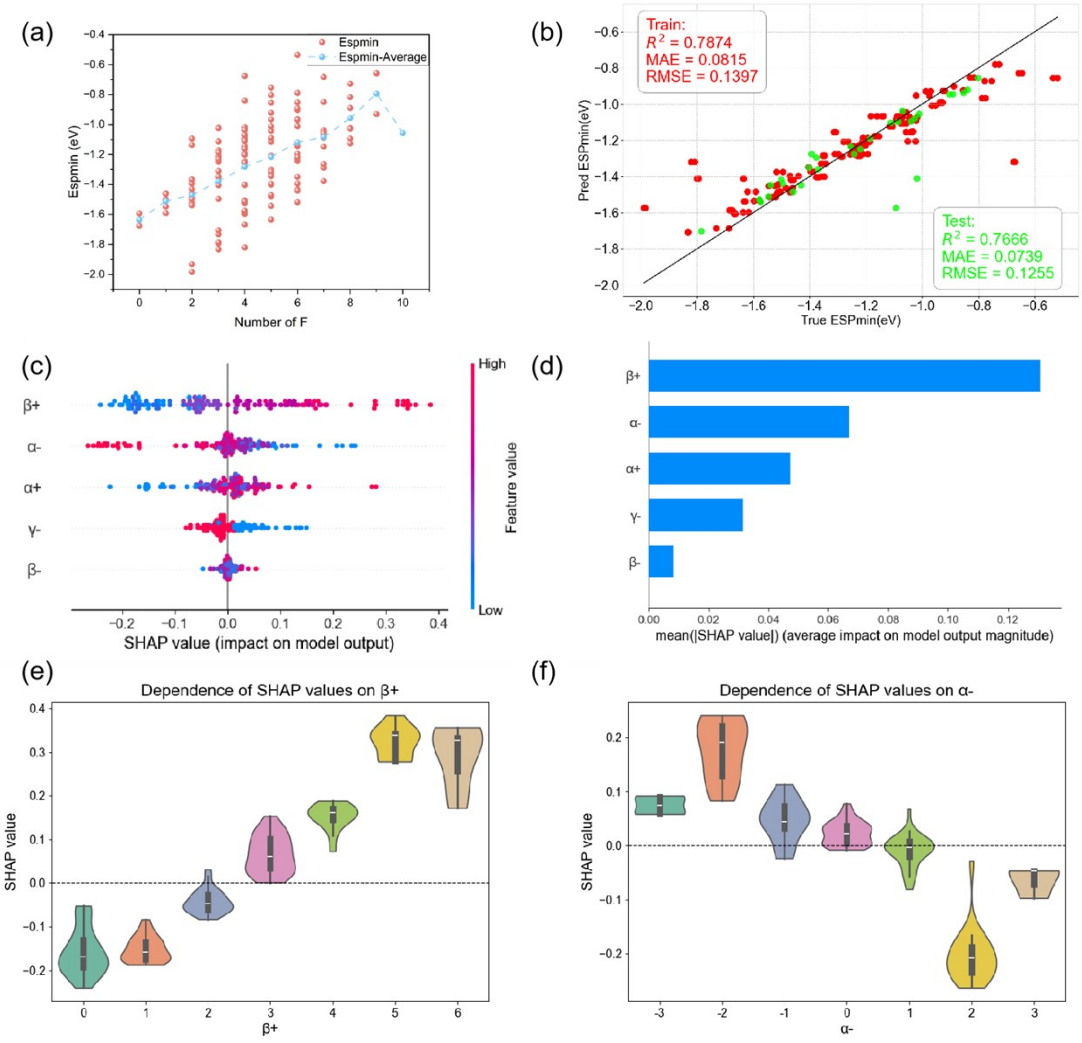

Fig. S30. XGBoost model fitting for the Minimum surface electrostatic potentials of the CFs. (a) Distribution of minimum surface electrostatic potentials under different fluorination conditions. (b) Performance of the machine learning model in fitting and predicting minimum surface electrostatic potentials (with red and green dots representing the training and testing datasets, respectively). (c) SHAP values for all input features, providing local interpretability of the machine learning model. (d) Importance ranking of all input features. (e) Dependence of SHAP values on β+. (f) Dependence of SHAP values on α-.

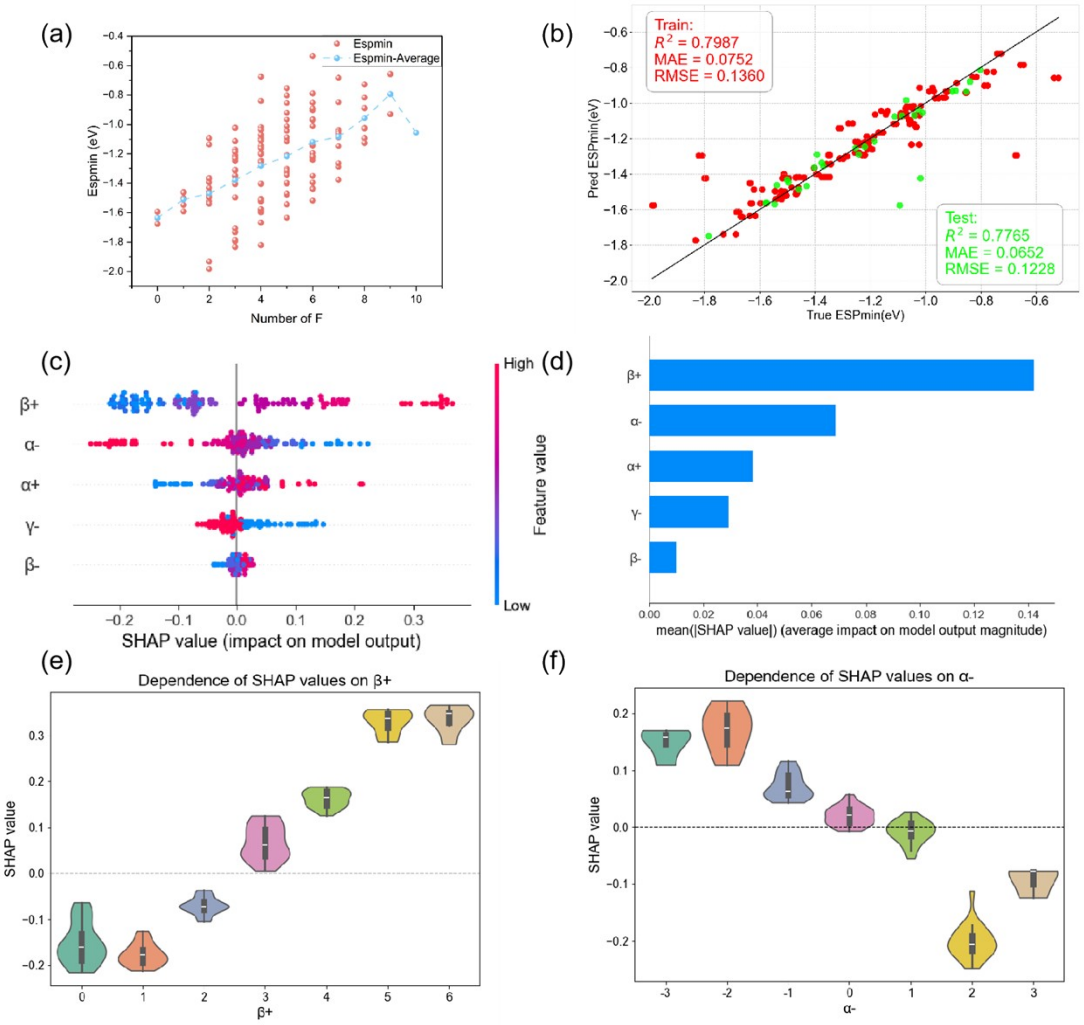

Fig. S31. RF model fitting for the Minimum surface electrostatic potentials of the CFs. (a) Distribution of minimum surface electrostatic potentials under different fluorination conditions. (b) Performance of the machine learning model in fitting and predicting minimum surface electrostatic potentials (with red and green dots representing the training and testing datasets, respectively). (c) SHAP values for all input features, providing local interpretability of the machine learning model. (d) Importance ranking of all input features. (e) Dependence of SHAP values on β+. (f) Dependence of SHAP values on α-.

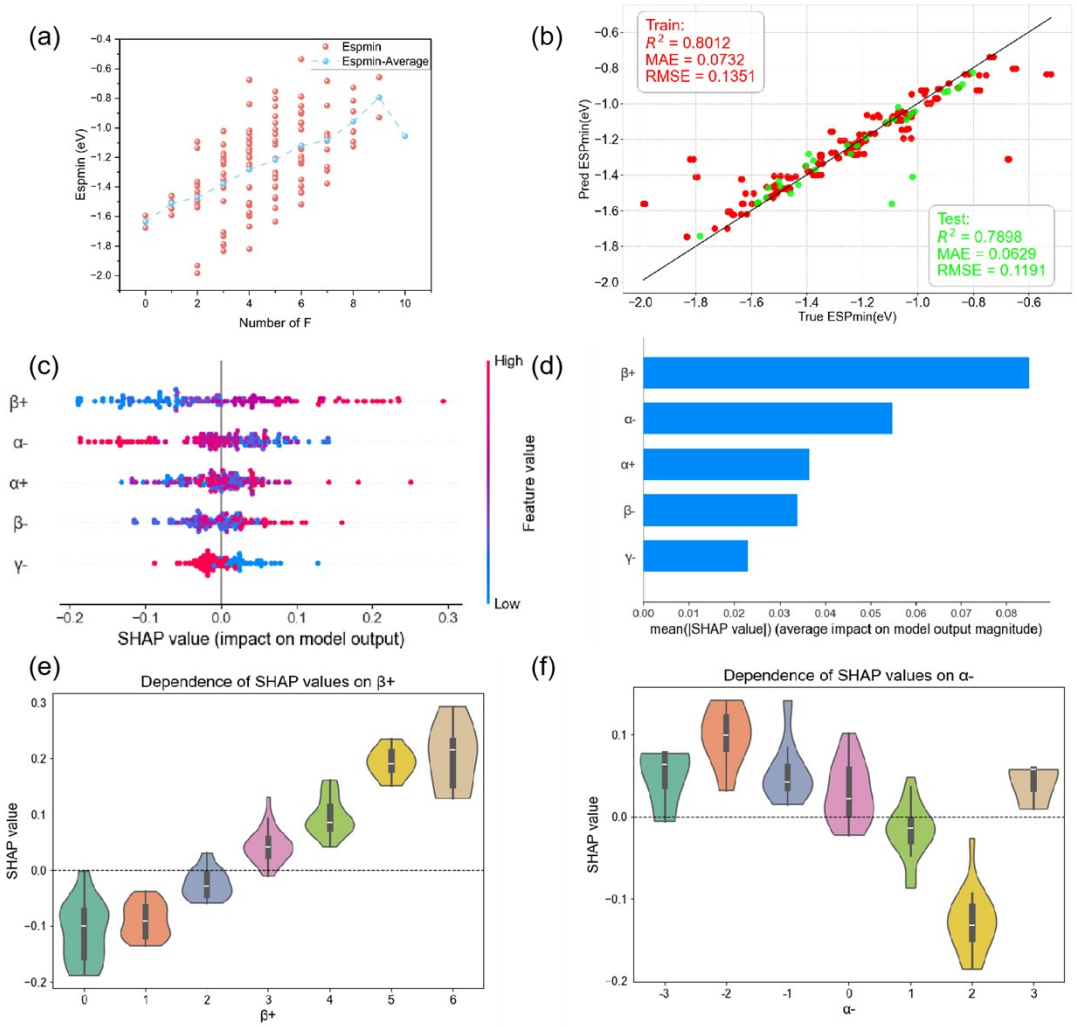

Fig. S32. SVR model fitting for the Minimum surface electrostatic potentials of the CFs. (a) Distribution of minimum surface electrostatic potentials under different fluorination conditions. (b) Performance of the machine learning model in fitting and predicting minimum surface electrostatic potentials (with red and green dots representing the training and testing datasets, respectively). (c) SHAP values for all input features, providing local interpretability of the machine learning model. (d) Importance ranking of all input features. (e) Dependence of SHAP values on β+. (f) Dependence of SHAP values on α-.

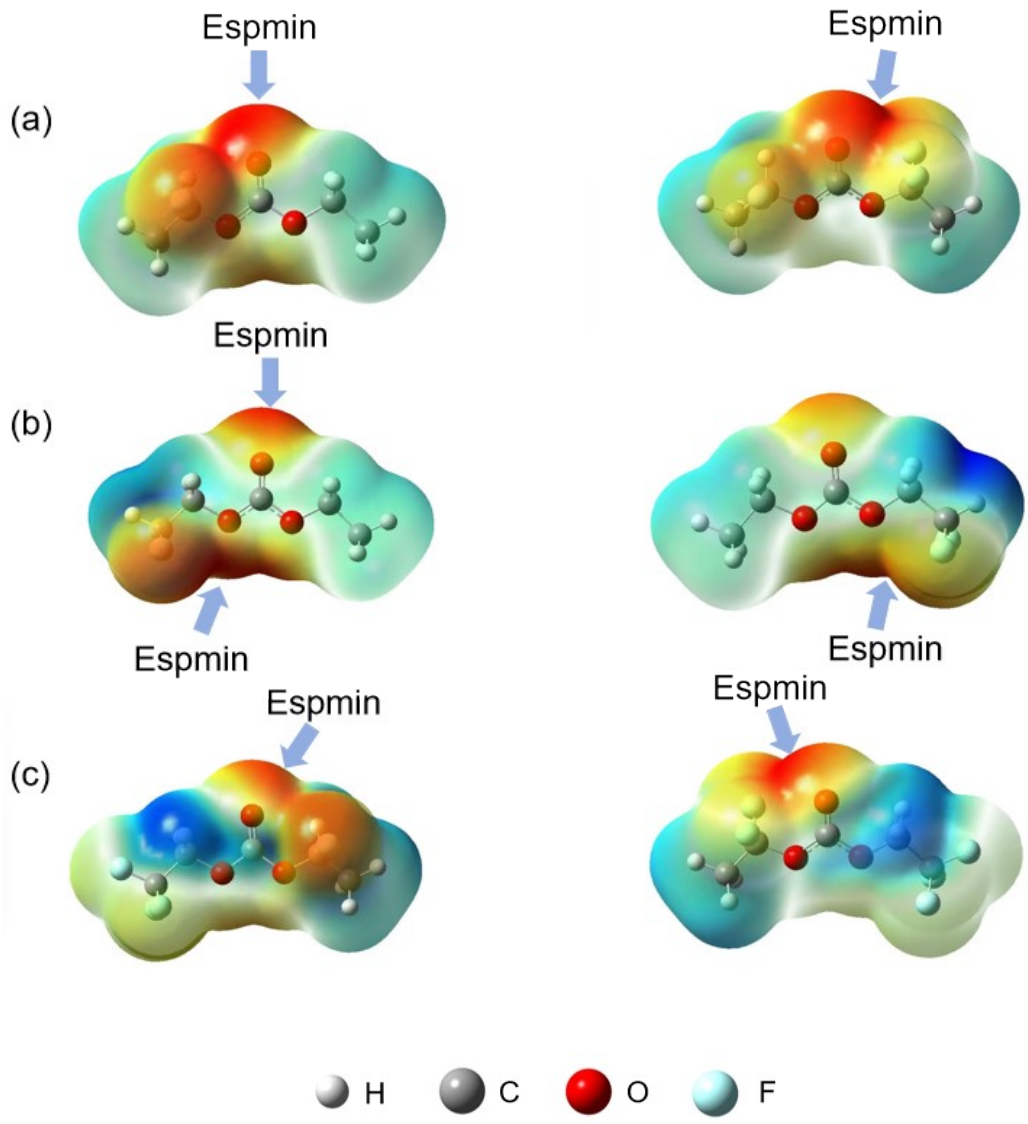

Fig. S33. ESP maps of partially fluorinated molecules. (a) Typical molecule with only α-fluorination; (b) Typical molecule with only β-fluorination; (c) Typical molecule with α,β-difluorination.

Table S2. Relationship between calculated descriptors, experimentally observable electrolyte behavior, and supporting literature.

Calculated descriptor	**Molecular-level meaning**	**Experimentally related behavior / metric**	**Representative supporting literature**	**Relevance to this work**
Oxidationpotential / ESW	Intrinsic resistance to oxidative decomposition	LSV / CV oxidative onset; high-voltage cathode tolerance; CEI stability; high-voltage cycling	1-3	Supports the use of thermodynamic-cycle-derived Eox and ESW as intrinsic oxidative-stability descriptors

Reduction potential	Tendency to acceptelectrons and undergoreductive decomposition	CV reductive peak; preferential reduction; initial SEI formation	1,2,5	Supports the use of Ered to evaluate reductive decomposition and possible film-forming tendency
HOMO / LUMO	Frontier orbital levels related to electron donation/acceptance tendency	Qualitative oxidative/reductive stability; interfacial decomposition tendency	1,4	Used as auxiliary electronic-structure descriptors rather than sole ECW predictors
Li^+ binding energy	Strength of solvent-Li^+ coordination	Solvation structure; desolvation behavior; Li^+ transport; Li deposition reversibility; Coulombic efficiency	3,4	Supports the link between Li^+ coordination strength and practical electrolyte behavior
Dipole moment	Molecular polarity and charge-distribution asymmetry	Interfacial adsorption tendency; wettability; ionic transport behavior	4	Used to evaluate polarity and possible interfacial orientation of fluorinated carbonates
ESPmin / ESPmax	Electron-rich / electron-poor regions on molecular surface	Possible reduction/oxidation sites; interfacial reaction selectivity; SEI/CEI chemistry	2,3	Used to identify potential interfacial reaction regions and electronic redistribution induced by fluorination
Fluorination degree / fluorination site	C–F bond introduction, inductive effect, local polarity modulation	Fluorinated interphase; LiF-containing SEI; cycling stability; Coulombic efficiency	2,4,5	Supports the site-specific analysis of α/β fluorination and fluorination asymmetry in this work

Table S3. Definitions, values, and physicochemical significance of multidimensional molecular feature descriptors.

Molecular feature descriptor	Value	Physicochemical Significance
α+	0, 1, 2, 3, 4, 5, 6	Total fluorine substitutions on the two alkoxy α-carbon atoms, reflecting the overall fluorination degree at the α position and its influence on the local electronic environment due to its proximity to electronegative oxygen atoms
α-	-3, -2, -1, 0, 1, 2, 3	Difference in fluorine substitutions between the left and right alkoxy α positions, reflecting molecular asymmetry at the polarity center and its influence on the physical properties of linear carbonates
β+	0, 1, 2, 3, 4, 5, 6	Total fluorine substitutions on the two alkoxy β-carbon atoms, reflecting the overall fluorination degree at the β position, where electronic effects are weaker than at the α position
β-	-3, -2, -1, 0, 1, 2, 3	Difference in fluorine substitutions between the left and right alkoxy β positions, reflecting β-position asymmetry and its contribution to overall molecular symmetry and properties
γ-	-1, 0	Difference in methyl substitutions at both ends of the carbon chain, reflecting terminal-chain asymmetry and distinguishing different linear carbonates (DMC, EMC, and DEC)

Table S4. Internal benchmark values used for calibrating the screening thresholds.

Molecule / criterion	Eox / V	Ered / V	Li^+ binding / eV	Dipole / D	S_vdW / $Å^{-1}$
DMC	7.07	-0.46	-1.87	0.4	1.147
EMC	6.91	-0.49	-1.93	0.63	1.113
DEC	6.84	-0.50	-1.95	0.66	1.089
Solvent criterion	>7.5	<0.5	-1.65 to -1.20	2.5-5.5	-
Additive criterion	-	>1.0	moderate	-	>1.1

Table S5. Theoretically prioritized solvent/additive candidates and related experimental precedents of fluorinated carbonate motifs.

Category	Candidate numbers in this work	Structural motif identified by screening	Screening/design rationale	Related experimental precedent
Bulk solvent candidates	**18-2, 18-13, 19-8**	DEC-derived / bis(fluoroethyl) carbonate-type structures	High oxidative stability, solvent-like reductive stability, moderate Li^+ binding, and suitable polarity	**6,7**
Solvent design principle	18-2, 18-13, 19-8	Partial fluorination with retained C–H bonds	Avoiding over-fluorination while maintaining oxidative stability and Li^+ solvation regulation	**8**
SEI-forming additive candidates	**3-1, 4-1, 5-1, 6-1**	DMC-derived short-chain trifluoromethyl carbonate motifs	High reduction tendency, compact molecular geometry, and favorable interfacial coverage	**9**

SEI-forming additive candidates	**9-1, 10-2, 11-1, 11-2, 11-9**	EMC-derived ethyl/trifluoromethyl carbonate motifs	High reduction tendency, compact geometry, and experimentally accessible EMC-derived fluorinated motif	**8,9**

Note: The literature examples summarized here are used to support the experimental relevance and synthetic accessibility of the identified fluorinated carbonate motifs. They do not indicate that the exact molecules predicted in this work have already been experimentally validated as electrolyte formulations.

1. D. Wang, T. He, A. Wang, K. Guo, M. Avdeev, C. Ouyang, L. Chen, S. Shi, *Advanced Functional Materials*, 2023, 33(11): 2212342.
2. X. Fan, L. Chen, O. Borodin, X. Ji, J. Chen, S. Hou, T. Deng, J. Zheng, C. Yang, S. C. Liou, K. Amine, K. Xu, C. Wang, *Nature nanotechnology*, 2018, 13(8): 715-722.
3. J. Zhang, H. Zhang, S. Weng, R. Li, D. Lu, T. Deng, S. Zhang, L. Lv, J. Qi, X. Xiao, L. Fan, S. Geng, F. Wang, L. Chen, M. Noked, X. Wang, X. Fan, *Nature Communications*, 2023, 14(1): 2211.
4. M. Qin, Z. Zeng, F. Ma, C. Gu, X. Chen, S. Cheng, J. Xie, *ACS Energy Letters*, 2024, 9(6): 2536-2544.
5. T. Hou, G. Yang, N. N. Rajput, J. Self, S. W. Park, J. Nanda, K. A. Persson, *Nano Energy*, 2019, 64: 103881.
6. S. Tan, O. Borodin, N. Wang, D. Yen, C. Weiland, E. Hu, *Journal of the*

American Chemical Society, 2024, 146(44): 30104-30116.

7. M.B. Shemirani, F. Gebert, A.J. Naylor, *RSC Applied Interfaces*, 2025, 2(3): 764-771.
8. Z. Yu, W. Yu, Y. Chen, L. Mondonico, X. Xiao, Y. Zheng, F. Liu, S.T. Hung, Y. Cui, Z. Bao, *Journal of The Electrochemical Society*, 2022, 169(4): 040555.
9. J. Han, C. Park, D. Jin, S. Kim, C.B. Dzakpasu, S. Lee, Y.M. Lee, *The Electrochemical Society*, 2023, 170(2): 020529.